Astronomy & Astrophysics manuscript no. main
October 15, 2019

The luminous and rapidly evolving SN 2018bcc:

Clues toward the origin of Type Ibn SNe from the Zwicky Transient Facility

E. Karamehmetoglu[1], C. Fransson[1], J. Sollerman[1], L. Tartaglia[1], F. Taddia[1], K. De[2], C. Fremling[2], A. Bagdasaryan[2], C. Barbarino[1], E. C. Bellm[5], R. Dekaney[3], A. M. Dugas[2], M. Giomi[8], A. Goobar[6], M. Graham[2], A. Ho[2], R. R. Laher[4], F. J. Masci[4], J. D. Neill[2], D. Perley[2], R. Riddle[3], B. Rusholme[4], and M. T. Soumagnac[7]

[1] The Oskar Klein Centre, Department of Astronomy, Stockholm University, AlbaNova, 10691 Stockholm, Sweden.
e-mail: emir.k@astro.su.se
[2] Division of Physics, Mathematics, and Astronomy, California Institute of Technology, Pasadena, CA 91125, USA.
[3] Caltech Optical Observatories, California Institute of Technology, Pasadena, CA 91125, USA.
[4] IPAC, California Institute of Technology, 1200 E. California Blvd, Pasadena, CA 91125, USA.
[5] DIRAC Institute, Department of Astronomy, University of Washington, 3910 15th Avenue NE, Seattle, WA 98195, USA.
[6] Oskar Klein Centre, Department of Physics, Stockholm University, SE 106 91 Stockholm, Sweden.
[7] Benoziyo Center for Astrophysics, Weizmann Institute of Science, Rehovot, Israel.
[8] Humboldt-Universität zu Berlin, Newtonstraße 15, 12489 Berlin.

Received XXX; accepted XXX

ABSTRACT

Context. Type Ibn supernovae (SNe) are rapidly-evolving and luminous ($M_{R,peak} \sim -19$) transients interacting with He-rich circumstellar material (CSM). SN 2018bcc, detected by the ZTF shortly after explosion, provides the best constraints on the shape of the rising lightcurve of a fast Type Ibn.
Aims. We use the high-quality data set of SN 2018bcc to study observational signatures of the class. Additionally, the powering mechanism of SN 2018bcc offers insights into the debated progenitor connection of Type Ibn SNe.
Methods. Well-constrained lightcurve properties obtained from empirical models are compared with the literature. We fit the pseudo-bolometric lightcurve with semi-analytical models powered by radioactive decay and CSM interaction. The line profiles and emissivity of the prominent He I lines are modeled to study the formation of P-Cygni profiles and to estimate CSM properties.
Results. SN 2018bcc has a risetime to peak of $5.6^{+0.2}_{-0.1}$ days in the rest frame with a rising shape powerlaw index near 2, and seems to be a typical rapidly-evolving Type Ibn SN. The spectrum lacks signatures of SN-like ejecta and is dominated by over 15 He emission features at 20 days past peak, alongside Ca and Mg, all with $V_{FWHM} \sim 2000$ km s^{-1}. The luminous and rapidly-evolving lightcurve can be powered by CSM interaction but not by the decay of radioactive ^{56}Ni. Modeling of the He I lines indicates a dense and optically thick CSM that can explain the P-Cygni profiles.
Conclusions. Like other rapidly-evolving Type Ibn SNe, SN 2018bcc is a luminous transient with a rapid rise to peak powered by shock-interaction inside a dense and He-rich CSM. Its spectra do not support the existence of two Type Ibn spectral classes. We also note the remarkable observational match to pulsational pair instability (PPI) SN models.

Key words. supernovae: general – supernovae: individual: SN 2018bcc, SN 2006jc, ZTF18aakuewf

1. Introduction

Supernovae (SNe) Type Ibn and IIn are thought to be strongly interacting with the circumstellar material (CSM) surrounding their progenitor stars. The shocks created by the interaction between ejecta and CSM convert kinetic energy into radiation (e.g., Chevalier & Fransson 2017). The interaction also modifies the spectral features of SNe Ibn and IIn, as well as the luminosity and duration of their lightcurves (where one characterization of duration is risetime, often defined as the interval between the estimated explosion epoch and the peak of the lightcurve). The -n suffix represents the fact that Ibn and IIn SNe display strong and relatively narrow lines of He and H, respectively; presumably a direct signature of this interaction (e.g., Smith 2017).

Unlike the longer risetimes of the more common Type IIn SNe, several Type Ibn SNe have very fast lightcurves with risetimes of a few days followed by a similarly rapid decline (Hosseinzadeh et al. 2017). Such rapidly evolving lightcurves make fast Type Ibn SNe[1] a member of the mysterious group of short-duration extragalactic transients (Whitesides et al. 2017). This part of the phase space of optical transients is both interesting and yet poorly constrained, due to the observational biases against detection (Kasliwal 2012). For example, the discovery of the kilonova AT2017gfo (Coulter et al. 2017; Kasliwal et al. 2017; Arcavi et al. 2017; Nicholl et al. 2017), the optical counterpart to the double neutron-star merger event GW170817(Abbott et al. 2017a,b), was a fast, faint, and rare event located in this area of phase space. Other rare classes of transients in this fast part of the phase space have also been recently discovered, such as Fast-Blue Optical Transients (FBOTs; e.g., Drout et al. 2014), which the mysterious extreme object AT2018cow (Perley et al. 2019) is a likely a member of. In fact, Fox & Smith (2019) sug-

[1] By "fast Type Ibn SNe" we mean rapidly evolving members of this class with risetimes $\lesssim 1$ week.

gest in their recent paper that AT2018cow might be related to Type Ibn SNe.

In this paper we highlight the possibility of using the Zwicky Transient Facility (ZTF), a state-of-the-art wide-field robotic transient survey, to find and follow-up rapidly evolving explosive transients by focusing on the example of SN 2018bcc, which is a fast-rising Type Ibn SN detected during early survey operations (Fig. 1). Despite the rarity of Type Ibn SNe, ZTF was able to obtain the hitherto best example of a fast Type Ibn SN with a well-sampled rising lightcurve.

1.1. Type Ibn SNe

The classification of Type Ibn SNe was first proposed by Pastorello et al. (2007) to include H-poor stripped-envelope (SE) SNe with relatively narrow He (~2000 km s^{-1}) emission features, with the prototypical example being SN 2006jc (Pastorello et al. 2007; Foley et al. 2007; Pastorello et al. 2008). Type Ibn SNe are relatively blue and bright at peak compared to an ordinary SE SN (Pastorello et al. 2016). The brightness, blue color, and the relatively narrow He emission features are all thought to be evidence of CSM interaction with a He-rich CSM, which could potentially be the primary powering mechanism of this class (see e.g., Pastorello et al. 2016; Hosseinzadeh et al. 2017; Karamehmetoglu et al. 2017).

To-date, no more than ~30 Type Ibn SNe have been published in the literature (Hosseinzadeh et al. 2019). Most of them have been studied in sample papers by Pastorello et al. (2016, P16) and Hosseinzadeh et al. (2017, H17), which have uncovered several puzzling observational signatures.

H17 show that the class of Type Ibn SNe displays a surprisingly homogeneous photometric evolution for CSM interacting SNe. Nevertheless, in their earlier sample paper, P16 argue that the class shows a large heterogeneity in spectral and lightcurve characteristics, with both very fast and long-lasting examples (see e.g., Pastorello et al. 2015b; Karamehmetoglu et al. 2017, for fast and slow, respectively). Similarly, a whole gamut of spectral properties can be found in the Type Ibn class that range from those with spectra that look very much like Type Ib SN spectra to those that show a significant number of H emission lines (even though the He features dominate), making them intermediate cases between Type IIn and Type Ibn SNe. Although this heterogeneity was also acknowledged in H17, the Type Ibn SN lightcurves in their analysis still seem to be much more similar to each other than the lightcurves of Type IIn SNe. The relative photometric homogeneity can offer clues into the nature of the CSM around Type Ibn SNe. It also means that detailed study of a well-observed event can prove fruitful.

In another puzzling observational signature, H17 noted that the early He I line profiles of Type Ibn SN seem to cluster into two groups (primarily based on the strong He I λ 5876 emission line): one showing strong P-Cygni profiles and the other appearing primarily in emission. By 20 days past peak however, both groups had evolved to become more emission dominated. H17 suggested that this division could be a result of optical depth effects in the CSM. Since He I line profiles and fluxes depend on density, temperature, and optical depths (e.g., Fransson et al. 2014), their suggestion can be investigated by modeling the optical depth effects on the He I line profiles of Type Ibn spectra.

In the rest of this paper, we present the most well-constrained fast-rising Type Ibn SN, SN 2018bcc, and compare it to a selected literature sample. It has a < 6 d risetime as seen in Fig. 2 and declines on a similar time-scale as other Type Ibn SNe. While several examples of Type Ibn SNe with fast risetimes (<< 10 d) are known in the literature (see e.g., Pastorello et al. 2015b, H17), their rapid evolution and the rarity of Type Ibn SNe have resulted in few detections at or before peak. Consequently, observations defining the shape of the rising lightcurve have been lacking for these rapidly evolving events. Additionally, their rapid decline has also made it difficult to obtain late-time spectra.

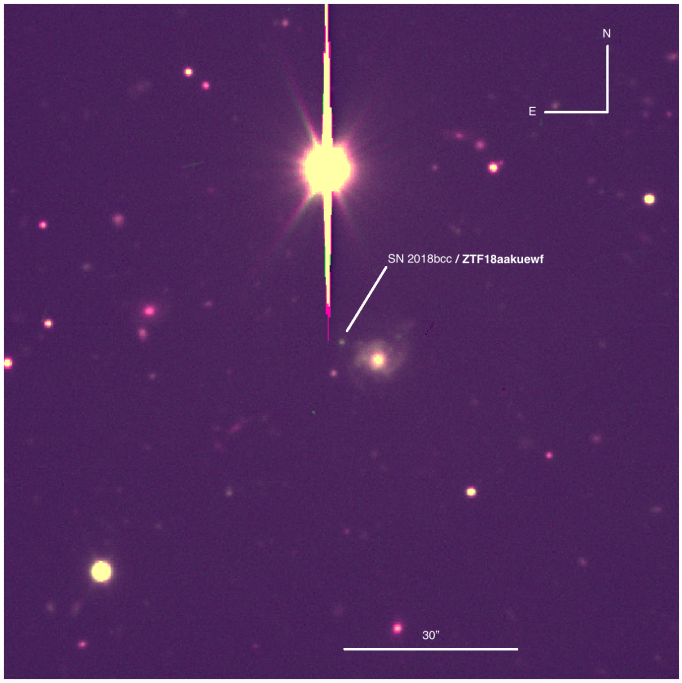

Fig. 1 Color-combined image of SN 2018bcc (g- and r-band filters from TNG+DOLORES) at the epoch of our last detection. North is up and East is to the left. The field-of-view is 2′x 2′. The SN, well visible at the center of the image, is located in the outskirts of its host galaxy. A bright, saturated star is positioned north and somewhat east of the host galaxy.

The paper is laid out as follows: Section 1.2 presents basic information about SN 2018bcc and its host. Section 2 describes the ZTF survey and contains the details of the photometry and spectroscopy that were obtained. The analysis of this data is presented in Sect. 3 followed by our semi-analytical modeling in Sect. 5.2. The results are presented in Sect. 6 and discussed in the context of Type Ibn SNe in Sect. 7. Finally we list our conclusions in Sect. 8.

1.2. SN 2018bcc

SN 2018bcc, located at RA = 16:14:22.65 and Dec = +35:55:04.4 (J2000.0), was first detected by the ZTF on 2018 April 18.34 (JD 2458226.84052) at an r-band magnitude of 18.98. ZTF previously observed this field 1.89 days before, on April 16.45, and could not detect any source down to a magnitude of $r > 20.12$ at the location of the transient. In the first three days after discovery, the SN was followed in r band only, and thereafter it was also imaged in g band.

In April 2018, the ZTF survey had begun public survey observations but the associated alert stream (Patterson et al. 2019)

had not yet started. The transient was subsequently discovered by ATLAS[2] on 2018 April 19, and by Gaia[3] 5 days later.

Milky Way (MW) extinction towards the SN is estimated to be E(B−V) = 0.0124 mag (Schlafly & Finkbeiner 2011). We did not detect evidence for significant host extinction (in the form of narrow Na ID absorption lines or a reddened spectrum) and assume it to be negligible for the analysis presented in this paper. Additionally, the SN is located in the outskirts of its host galaxy and is blue in color, which corroborates our assumption of insignificant host extinction. The redshift towards the SN is measured to be z = 0.0636 (Sect. 4) from a fit to the He emission lines of the SN, and verified via host galaxy emission lines present in the latest 2D spectrum. Assuming a cosmology with H_0 = 73 km s^{-1} Mpc^{-1}, Ω_M = 0.27, Ω_Λ = 0.73 (selected to enable easier literature comparisons), we calculate a distance modulus = 37.19 mag. This corresponds to a luminosity distance of 274 Mpc.

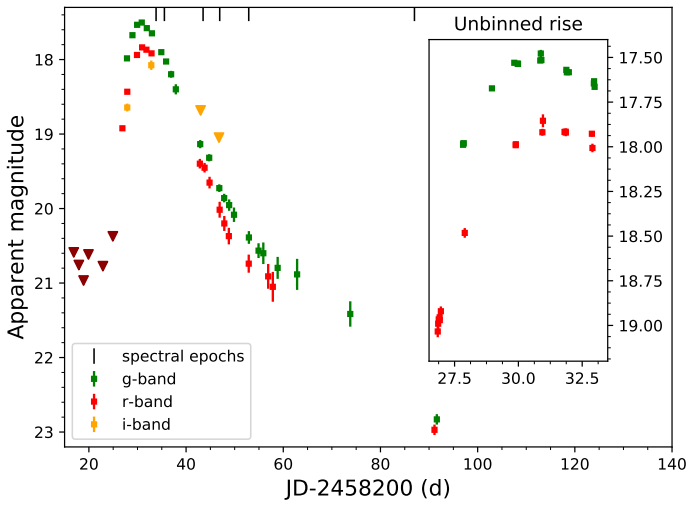

Fig. 2 Apparent magnitude lightcurve of SN 2018bcc, binned daily. The average magnitude of each bin was used with the errors added in quadrature. Limits are the deepest limit for the night. The observations are from the P48 survey telescope except for the final *g* and *r*-band detections, which were obtained with the TNG. The spectral epochs are indicated with vertical black dashes at the top of the figure. **Inset:** A zoomed-in version of the unbinned rising lightcurve, highlighting the well-captured rise in the *r* band.

2. Observations

2.1. The Zwicky Transient Facility (ZTF)

Building on the success of previous transient surveys, the next-generation synoptic surveys such as the Zwicky Transient Facility (ZTF; Bellm et al. 2019b; Graham & Zwicky Transient Facility (ZTF) Project Team 2018), the successor to the (i)PTF, have come online. The ZTF[4] is a state-of-the-art robotic survey conducted on Palomar Samuel Oschin 48-inch (1.2 m) Schmidt Telescope with a 47 deg^2 effective field-of-view. In the standard configuration, the survey takes 30 s exposures reaching down to ~21st magnitude in the *r* band with 10 s instrument overheads and a dedicated robotic scheduler that minimizes slewing overheads (Bellm et al. 2019a). Essentially, the ZTF can survey the entire northern sky above Palomar every night down to 21st magnitude (Bellm et al. 2019b).

The ZTF survey has been optimized for transient science (Bellm 2016) by both covering the entire night sky with a ~3 day cadence in *g* and *r* bands while also covering smaller parts of the sky with 2–4 observations per night in the two filters. As a result, the ZTF survey provides an opportunity to populate some of the remaining gaps in the the brightness and duration phase-space of transients, especially with respect to discovering and obtaining well-sampled lightcurves for rare and fast objects such as Type Ibn SNe.

2.2. Photometry

We collected photometry in *g*, *r*, and *i* bands from the ZTF survey obtained with the P48 telescope[5]. The ZTF pipeline is described in Masci et al. (2019) and employs the image subtraction algorithm of Zackay et al. (2016). We also obtained late-time images in *g* and *r* bands using the 3.58m Telescopio Nazionale Galileo (TNG)[6].

The P48 photometry was reduced using FPipe (Fremling et al. 2016), which produces point-spread function (PSF) photometry from sky and template subtracted images. The final photometric reduction was done using reference templates obtained by stacking images from more than 2 weeks before discovery (JD < 2458209) to remove any possibility of SN light contributing to the template. FPipe photometry is converted to the SDSS photometric system using reference stars in the field selected from the Pan-STARRS 1 survey (Magnier et al. 2016; Flewelling et al. 2016).

The final epoch of images obtained with the TNG were reduced using standard IRAF[7] photometric reduction steps without template subtraction (since the galaxy is better resolved with the TNG).

SN 2018bcc was detected very early in the ZTF public survey. Some of the data were obtained during verification of subsystems. During normal operations the ZTF lightcurves would be more evenly sampled but here we actually obtained an unusually high sampling during the first night. The photometry for the alerts has since been improved upon, and alert distribution in the public survey began to be published in June 2018. We work only with re-reduced photometry from FPipe in this paper.

2.3. Spectroscopy

A log of the spectral observations is presented in the Appendix, Table C.1 and the spectral sequence is show in Fig. 3. An initial spectrum was obtained 6.99 d after discovery with the Palomar 60 inch (P60) telescope (Cenko et al. 2006) equipped with the SED machine (SEDM; Blagorodnova et al. 2018; Rigault et al. 2019). Since the SEDM spectrum showed a featureless blue spectrum, an additional classification spectrum was obtained using the SPectrograph for the Rapid Acquisition of Transients (SPRAT) mounted on the Liverpool Telescope (LT; Steele et al. 2004). Relatively low resolution but automated spectroscopic

[2] https://wis-tns.weizmann.ac.il/object/2018bcc/discovery-cert
[3] https://wis-tns.weizmann.ac.il/object/2018bcc
[4] http://ztf.caltech.edu
[5] The ZTF filter profiles can be found at: https://github.com/ZwickyTransientFacility/ztf_information
[6] The photometry is made available publicly via <give link to photometry on WiseRep in final version>
[7] Image Reduction and Analysis Facility.

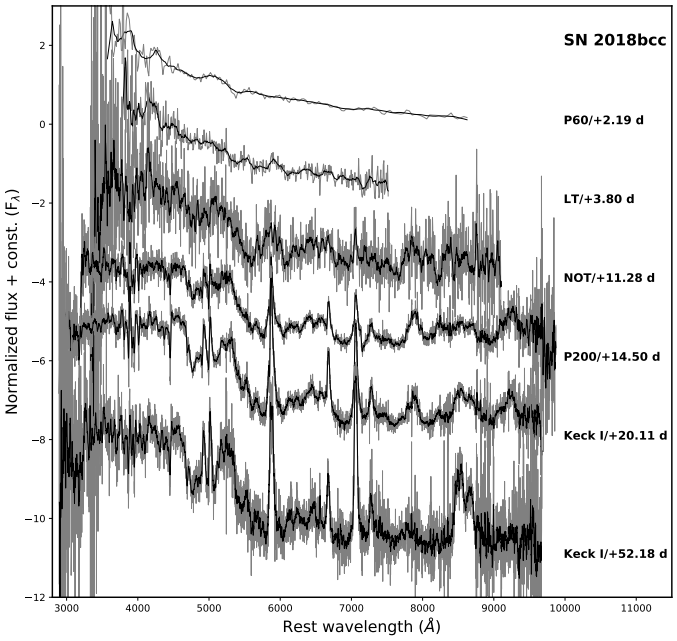

Fig. 3 Spectral sequence for SN 2018bcc with restframe phase since peak (JD 2458231.5) of each spectrum indicated. The original spectrum is shown in gray while solid black lines represent the binned data.

follow-up instruments such as the SEDM and SPRAT are the primary means by which ZTF classifies extragalactic transients (Fremling et al. 2018).

Additional follow-up spectra were obtained with Keck I equipped with LRIS (Low Resolution Imaging Spectrometer; Oke et al. 1995; Perley 2019), the Nordic Optical Telescope (NOT) equipped with ALFOSC (The Alhambra Faint Object Spectrograph and Camera), and the Palomar 200 inch (P200) telescope equipped with DBSP (the Double Spectrograph; Oke & Gunn 1982; Bellm & Sesar 2016). The spectra are made publicly available via WiseRep (Yaron & Gal-Yam 2012).

The spectra were reduced by members of the ZTF collaboration in a standard manner with dedicated pipelines for each instrument. In general, the spectra are bias and flat-field corrected, wavelength calibrated using an arc spectrum, extracted and then flux calibrated using a sensitivity function obtained from observing spectrophotometric standard stars. We further absolute flux calibrate the spectra by comparing synthetic photometry computed from the spectra to our *r*-band photometry.

The synthetic photometry were computed using synphot (STScI development Team 2018) and the PS1 filter profiles since our photometry were calibrated to PS1[8]. The spectra were then de-reddened to correct for MW extinction using E(B−V) = 0.0124 mag and $R_V = 3.1$, as for the photometry.

3. Photometric Analysis

Restframe absolute magnitude lightcurves for SN 2018bcc are constructed using the previously mentioned distance modulus. Correction for extinction due to the MW is applied while host extinction is assumed to be negligible (Sect. 1.2). We compare this lightcurve in *g* and *r* bands to a literature sample of Type Ibn SN lightcurves in Fig. 4. In the comparison sample we include all of the fast rising Type Ibn SNe with a meaningful constraint on the rise: LSQ12btw and LSQ13ccw (Pastorello et al. 2015b); PTF12ldy, iPTF14aki, and iPTF15ul (Hosseinzadeh et al. 2017). We also include the well-observed but much slower SN 2010al (Pastorello et al. 2015a), the prototypical example of the Type Ibn class - SN 2006jc (Pastorello et al. 2007; Foley et al. 2007), and the very nearby Type Ibn SN 2015U (Shivvers et al. 2017) for comparison. The template Type Ibn R-band lightcurve from Hosseinzadeh et al. (2017) is also shown. The literature sample has been corrected for MW extinction and we adopt explosion epochs, distance moduli, and redshifts as estimated by the respective works. In the cases of iPTF15ul and SN 2015U, where significant evidence of host extinction was noted and estimated, we also correct for the host extinction as reported in these papers. We note that without correcting for significant host extinction, iPTF15ul would be similar in brightness to other Type Ibn SNe, including SN 2018bcc.

SN	Rise (restframe d)	Uncertainty (d)	Powerlaw α
SN 2018bcc	5.6	$^{+0.2}_{-0.1}$	1.95 ± 0.22
iPTF15ul	4.0 [3.0]	±0.6 [0.7]	1.8 ± 0.4
LSQ13ccw	[4.7]	±[2.1]	-
LSQ12btw	[< 3.8][a]	-	-
PTF12ldy	[6.2]	±[2.0]	-

[a]Peak cannot be determined.

Table 1 Risetime and powerlaw rising shape of fast Type Ibn SNe, with literature values in square brackets. Calculation of the risetime and the powerlaw fits to obtain the index α for SN 2018bcc and iPTF15ul were performed by us in Sect. 3.1. The remaining literature data were taken from the sample paper by Hosseinzadeh et al. (2017).

3.1. Risetime

The risetime is the interval between the estimated explosion and peak epochs. Although SN 2018bcc has a fast risetime similar to a few other Type Ibn SNe, the nature of the ZTF observations allowed us to capture an unusually well-sampled rising lightcurve, with seven photometric points on the first day and well-sampled g, r band data on the rise, peak, and decline- the combination of which has not been observed for such a fast-rising Type Ibn SN before (see Fig. 4 for a comparison to other Type Ibn SNe). The well-defined peak epoch and close pre-discovery limits of SN 2018bcc allow us to establish a well determined risetime; a unique opportunity for a fast Type Ibn SN (Table 1). We perform this exercise using the $r-$band lightcurve.

In order to quantify the shape of the rising lightcurve, a low-order polynomial fit was used to obtain the epoch of the peak of the $r-$band lightcurve: JD 2458231.5, which we use as reference phase in the rest of the paper. (The $g-$band peaks slightly before on JD 2458230.9.) The binned lightcurve was put into flux space using the AB-magnitude zero point, with the upper limits shown at zero flux and error bars corresponding to the measured limits. Then, we estimated the explosion epoch and the corresponding risetime (in restframe) in four different ways.

[8] Obtained from the Spanish Virtual Observatory Filter Profile Service (SVO), http://svo2.cab.inta-csic.es/theory/fps3/index.php

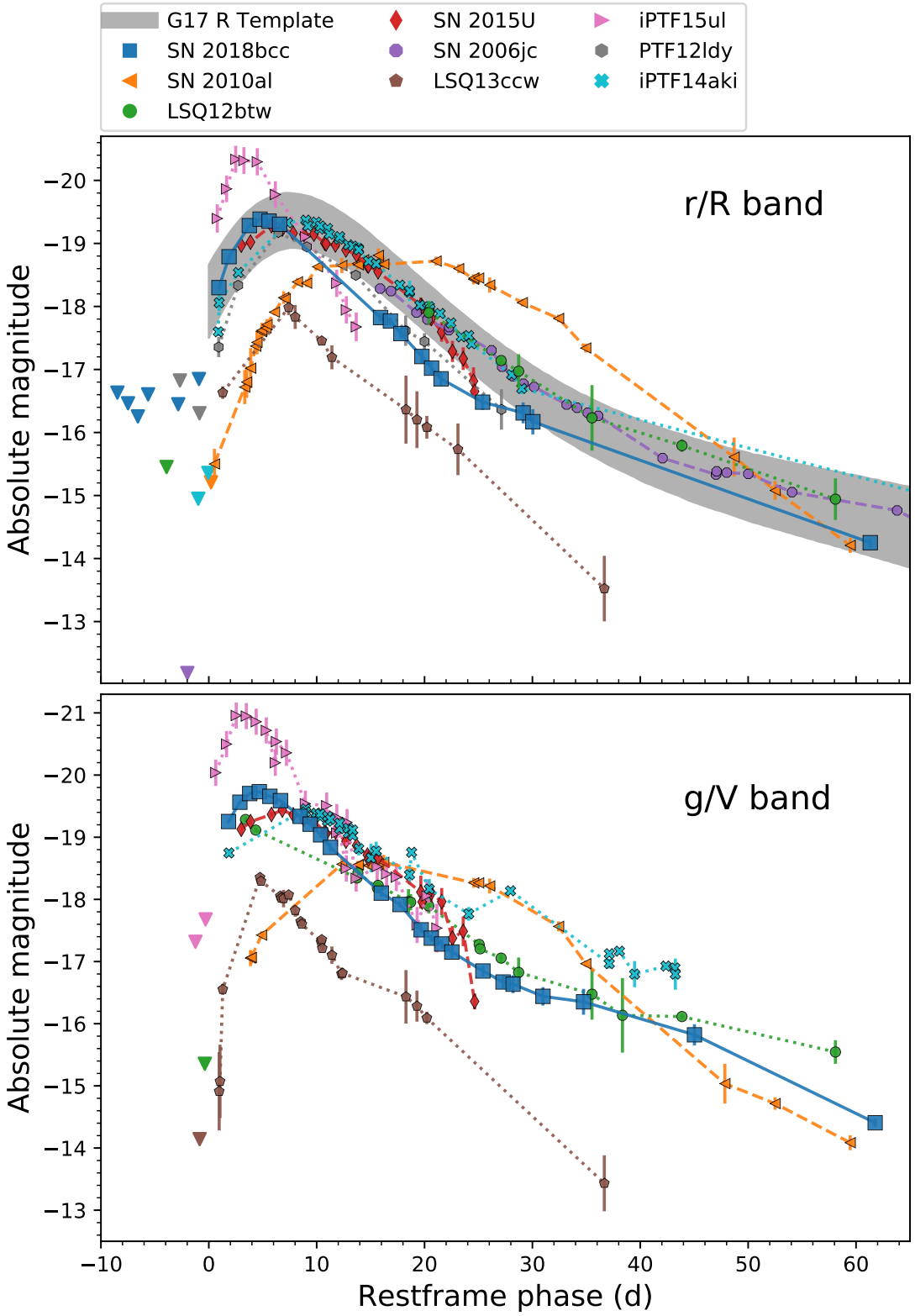

Fig. 4 Restframe absolute magnitude lightcurve comparison of SN 2018bbc (binned daily) to the literature comparison sample (Sect. 3). SN 2018bbc is shown with a blue line, the fast-rising SNe are shown with dotted lines, and the other Type Ibn SN lightcurves are shown with dashed lines. **The upper panel** shows the *r*/R band while **the lower panel** contains the *g*/V-band lightcurves. The lightcurves are plotted relative to estimated explosion epoch and their respective pre-discovery limits are also shown with triangles. They have been corrected for redshift, MW, and host extinction (where appropriate). The R-band Type Ibn template from Hosseinzadeh et al. (2017) is plotted for comparison, with the phase given since the first available template point.

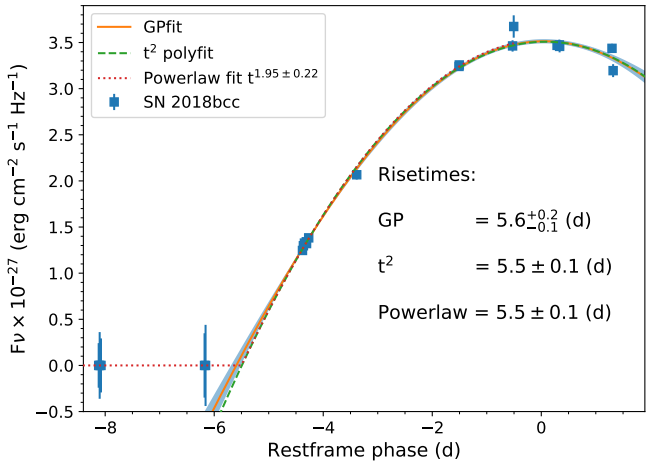

Fig. 5 Estimating the restframe risetime from fits with $\propto t^2$, a more general t^α powerlaw, and using Gaussian process regression, to the rising lightcurve extrapolated to zero flux.

Most conservatively, the risetime is estimated to be the average of the last upper limit and first detection (JD 2458226.8), yielding 5.1 ± 1.0 days, with the uncertainty given by the period between last non-detection and first detection. Second, we fit the rise in flux space with a t^2 scaling polynomial and extrapolate down to zero flux. Assuming that the explosion epoch approximately corresponds to the epoch where the fit crosses zero flux, this method yields a risetime of 5.5 ± 0.1 days. The same assumption is also made in the remaining two methods. Third, we fit a powerlaw of the form $[(t-t_{max})/t_{rise}]^\alpha$, allowing α to vary, and fitting the upper limits at the same time. We obtain $\alpha = 1.95 \pm 0.22$ and a corresponding risetime of 5.5 ± 0.1 days. Finally, we perform a non-parametric fit using Gaussian process (GP) regression, which has the benefit of learning the noise from the data. Extrapolating the GP fit to zero flux yields a risetime of $5.6^{+0.2}_{-0.1}$ days. The polynomial, powerlaw, and GP fits are plotted in Fig. 5. All four estimates of the risetime agree within the errors. For the rest of the paper, we use a risetime of $5.6^{+0.2}_{-0.1}$ days as calculated using the more conservative GP regression, which corresponds to an explosion epoch of JD 2458225.5.

The precise risetime and the shape of the rising lightcurve of SN 218bcc makes it the most well-observed example among fast Type Ibn SNe. Other fast-rising Type Ibn SNe had an uncertain peak epoch due to the difficulty of catching and sampling the peak for such rapidly evolving events. The risetimes and rising shapes of fast Type Ibn SNe are compared in Table 1. PTF15ul, the previously best observed example, was the only other fast Type Ibn SN for which we were able to obtain a meaningful constraint on the exponent of the powerlaw fit to the rise, $\alpha = 1.8 \pm 0.4$, and a risetime of 4.0±0.6 d using the powerlaw method. This was done in the same way as for SN 2018bcc above. The exponents obtained for the powerlaw fits to the two SNe agree within the uncertainties and are close to a value of 2.0 predicted by the simple fireball model, sometimes used for Type Ia SNe (e.g., Riess et al. 1999). It seems that the large sky coverage and high cadence of ZTF will enable us to obtain a sample of these rare and rapidly evolving events with well-observed peaks and risetimes, which has been lacking in previous investigations of fast-evolving Type Ibn SNe.

3.2. Colors

The restframe $g - r$ color evolution of SN 2018bcc is plotted in the right-hand panel of Fig. 6. The colors were obtained by interpolating the $r-$ and $g-$band absolute magnitude lightcurves using both a Contardo et al. (2000) empirical fit and smoothing splines. By using Gaussian process regression, the empirical fits were assumed to have normally distributed (white) noise around the fit. In addition, the fits were allowed to smoothly vary to better fit the data using a radial-basis kernel. This process allowed us to build a model that interpolates the full lightcurves and estimates the uncertainty more robustly, including phases of the lightcurve far away from photometric epochs (which naturally have larger uncertainties). The interpolation models are shown in the left-hand panel of Fig. 6 and these are used to calculate the $g - r$ color in the right-hand panel of the same figure.

The color is relatively blue with an evolution to the red that lasts until ∼2 weeks past discovery, after which the color seems to become bluer again, and finally it remains relatively flat within the estimated uncertainties. This is typical of Type Ibn SNe, which are usually quite blue at early times (Pastorello et al. 2016).

The results of the interpolation models differ when extrapolating the very early g-band lightcurve due to the assumptions of each model and the lack of data. However we find that this does not make a significant difference in our analysis. In addition to color, these interpolation models were used to absolute flux calibrate the spectra to the photometry at the spectral epochs and for interpolation of the $g - r$ color when constructing the pseudo-bolometric lightcurve (Sect. 5.1). Additionally, we calculate the peak absolute magnitude of SN 2018bcc from the interpolation models as -19.37 ± 0.03 mag in the r band and as -19.68 ± 0.03 mag in the g band.

3.3. Decline rates

We measure the decline rate parametrized by the magnitude drop in 15 days after peak (ΔM_{15}), as well as the late-time decline slope (s) of SN 2018bcc. For ΔM_{15}, the interpolation models from the previous section are used, yielding $\Delta M_{15}(r) = 2.25 \pm 0.01$ mag and $\Delta M_{15}(g) = 2.24 \pm 0.02$ mag. When estimating s, we fit a line to the binned lightcurves and only consider the points later than 15 and 20 days past peak, thus calculating two separate slope values, s_{15} and s_{20}, respectively. We obtain $s_{15}(r) = 0.066 \pm 0.003$ mag d^{-1} and $s_{15}(g) = 0.072 \pm 0.003$ mag d^{-1} when cutting before 15 days and $s_{20}(r) = 0.063 \pm 0.001$ mag d^{-1} and $s_{20}(g) = 0.066 \pm 0.002$ mag d^{-1} when cutting at 20 days past peak. Similar to other fast Type Ibn SNe, SN 2018bcc thus seems to decline rather rapidly with a late-time rate of ∼0.06–0.07 mag d^{-1} and has a ΔM_{15} that is almost twice as large as the typical value for Type Ia SNe.

4. Spectroscopic analysis

We determine the redshift from the relatively narrow lines in the supernova spectrum. Using the last Keck spectrum we measured the five strongest emission lines and identify these with strong He I emission. The deduced redshift is then $z = 0.06358 \pm 0.0007$, where the error is the standard deviation from the mean redshift from the five lines. We also checked this with the location of nearby Hα in the 2D spectrum of the last Keck spectrum. There is Hα from the host nucleus and a nearby H II region, as well as slightly blue shifted emission from the SN (that is resolved and not coming from the host, see Sect. 4.2. From this investigation

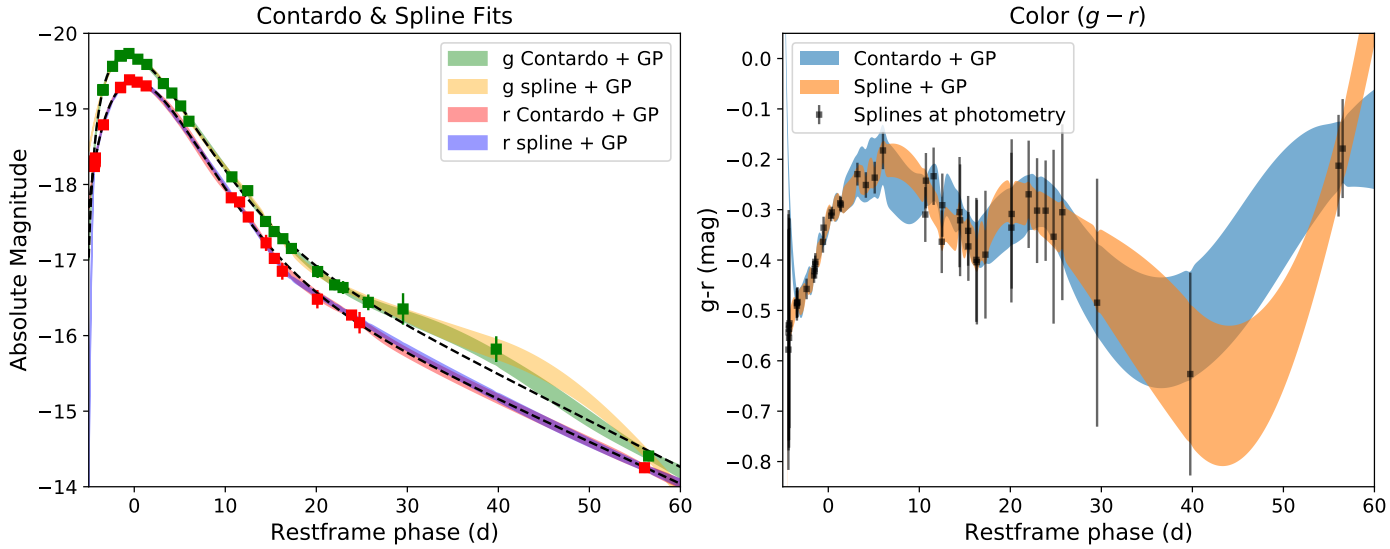

Fig. 6 **Left:** Empirical fits to the g and $r-$band lightcurves used for interpolation. The lightcurves were fit with both a purely empirical Contardo et al. (2000) model and with smoothing splines. Both these models were modified by a Gaussian process that allowed for both random noise and smooth deviations from the fits. The resulting models are used for interpolation. **Right:** Restframe $g - r$ color evolution of SN 2018bcc using the interpolations from the left panel. Both methods produce similar results. The black data points represent spline interpolation of the g and r bands to each other at the epochs of photometry with a linear interpolation of the photometric error added in quadrature.

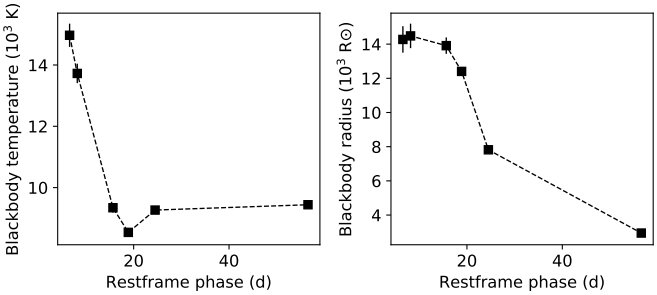

Fig. 7 **Left:** The evolution of the blackbody (BB) temperature obtained from BB fits to the spectra. **Right:** The evolution of the BB radius.

we obtain a slightly higher uncertainty of ±0.00098. The larger redshift error corresponds to a typical systematic uncertainty in our velocity measurements of ∼300 km s^{-1}.

Early spectra ($t \lesssim 10$ d past peak) show a blue featureless continuum, although the signal-to-noise ratio (SNR) is not sufficient to rule out the presence of shallow features. At these early phases the spectra are well fitted by a blackbody (BB) with a temperature of 1–1.5 × 10^4 K (see Fig. 7 for a plot of the BB temperature evolution). From +14d, we clearly identify the prominent and relatively narrow He I emission lines (FWHM ∼ 2000 km s^{-1}), marking SN 2018bcc as a Type Ibn SN. These later spectra are not well matched to a BB due to the presence of strong emission lines, and so the effective temperatures obtained from such fits are dubious.

We perform line identification on the two emission dominated Keck spectra at +20 and +52 days using common Type Ibn SN lines. The results are plotted in 8. In addition to the He II] lines that dominate the spectra, we also clearly see lines of Mg I, Mg II, Ca II, and late-time Hα, in addition to possible Fe II features (Sect. 4.2).

4.1. Evolution of the He I lines

He I lines are visible from +11 d, although they become more evident at later phases. At +14 d we identify common strong lines of He I $\lambda\lambda$ 3889, 4471, 5876, 6678, and 7065 in emission, all showing P-Cygni profiles with prominent emission components and a varying strength in absorption. Additionally, we used the strong lines of He tabulated by NIST[9] and overlaid those with a relative intensity ≥ 10 (where λ 5016 is 100) on the spectrum taken at +20 d, which is plotted with dark blue dashed-lines in Fig. 8. As we will discuss in Sect. 4.1, lab measurements are not appropriate for the conditions in SN 2018bcc and we only use the line list to guide spectral identification. Nevertheless, every single He I line from NIST in the wavelength range of our spectrum matches a prominent emission feature with a P-Cygni profile in the spectrum except for in the very edges of the spectrum (He I $\lambda\lambda$ 3013 and 9464), where the spectrum is too noisy (SNR < 1). We consider this strong evidence for the detection of 15 He I lines in the late spectra of SN 2018bcc: $\lambda\lambda$ 3188, 3820, 3889, 4026, 4121, 4388, 4471, 4713, 4922, 5016, 5048, 5876, 6678, 7065, 7281.

All He I lines show symmetric profiles with broad wings typical of interacting transients and generally attributed to Thomson scattering by free electrons in an unperturbed dense CSM. The evolution of these lines from +14 to +52 d is shown in Fig. 9. Fitting a combination of Lorentzian and Gaussian components (for the emission and absorption components, respectively) to the seven strongest He I observed profiles (Figs. 8 & 9) we infer

[9] National Institute of Standards and Technology, https://physics.nist.gov/PhysRefData/Handbook/Tables/heliumtable2.htm

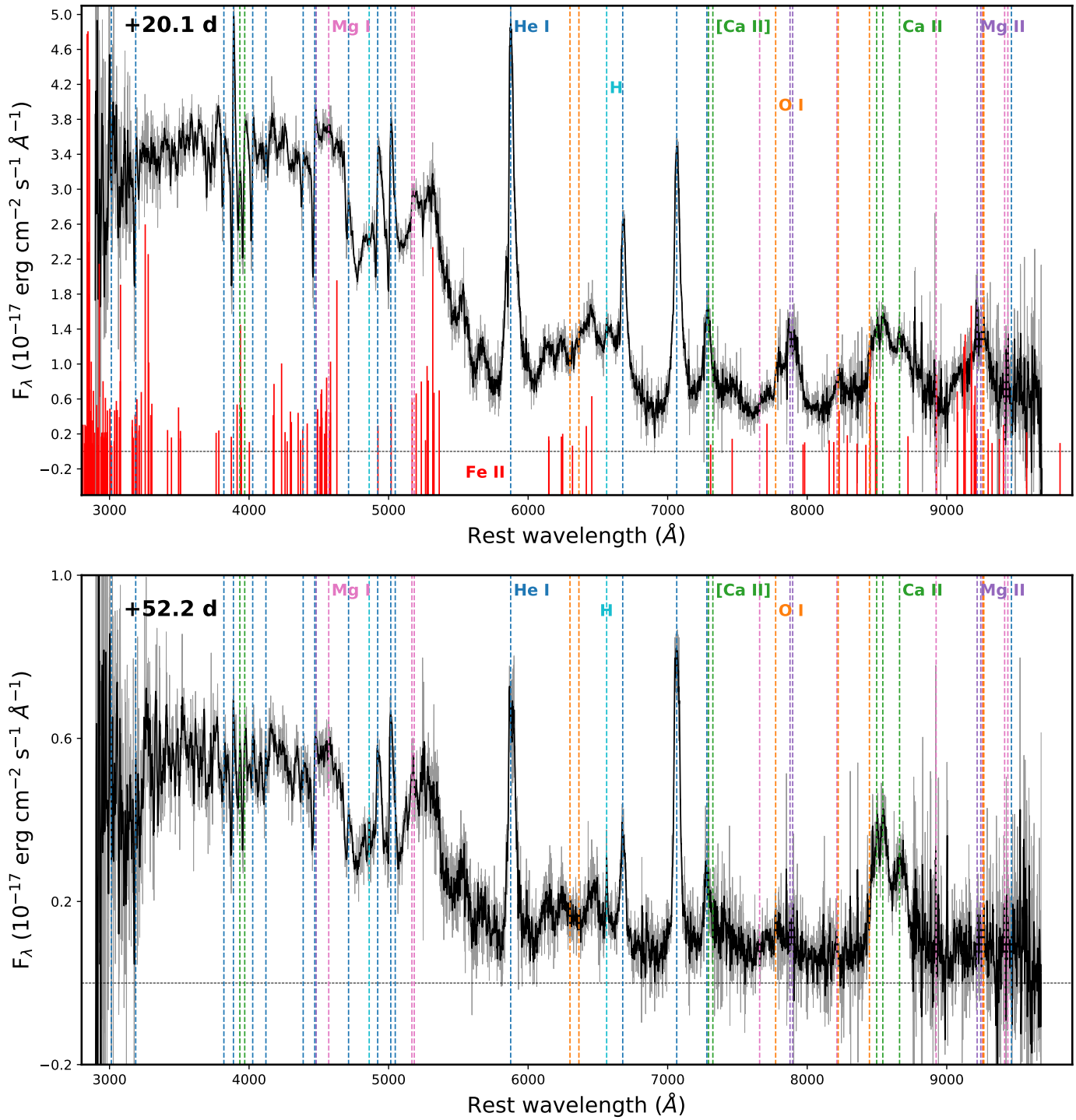

Fig. 8 **Upper**: Identification of lines present in the spectra. The prominent emission features are marked with dashed lines. Solid red lines show the location of possible Fe II features which could be contributing to the spectra. The height of these red lines indicates the expected relative strength of the line. **Lower:** Line identification carried onto the spectrum at +52 d.

FWHM that are nearly constant with time of 2370 ± 530 km s^{-1} for the emission components, while absorption features show blue wings extending up to 1600 ± 200 km s^{-1} and absorption minima of 960 ± 100 km s^{-1} (possibly representing expansion velocities).

At +20 d, He I λ 7065 still shows a FWHM $\simeq$ 2000 km s^{-1}, although the profile is well reproduced using a single Lorentzian component, without clear evidence of any absorption component, even though absorption components are clearly visible in other He I lines in the same spectrum. At +52 d, the He I lines evolve significantly; whereas He I $\lambda\lambda$ 3889 and 4471 lines still show P-Cygni profiles with pronounced absorptions and weak emission components, at redder wavelengths the lines are char-

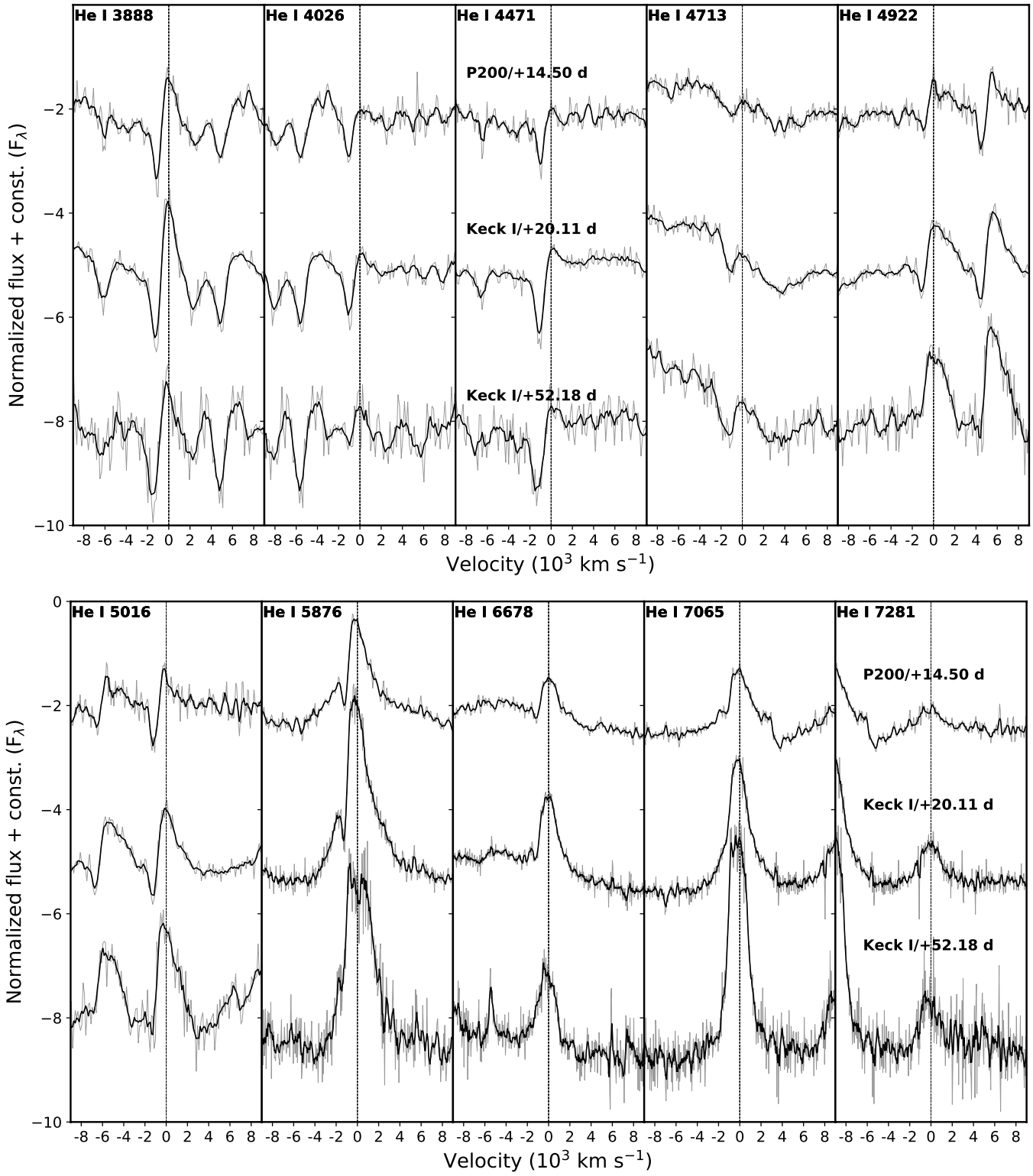

Fig. 9 The evolution of the ten prominent He I lines in the latter three spectra. The restframe line locations are indicated with vertical lines.

acterized by structured boxy profiles in emission with no trace of absorption.

In aggregate, the redder He I lines show weaker P-Cygni at earlier phases, but then evolve faster to show even less P-Cygni and more boxy profiles. Meanwhile, the P-Cygni profiles are stronger for bluer lines in the first spectrum, and while getting generally weaker in the latter spectra, still remain stronger than in the red lines and are still clearly visible at +52 d for the seven bluest lines (Fig. 8).

4.2. Identification and evolution of other lines

From +14 d, the spectra show an excess at wavelengths bluer than ∼ 5500 Å. These are most likely due to the presence of several Fe II multiplets (e.g. multiplets 40, 42, 46). To identify possible Fe II lines we use the calculation by Sigut & Pradhan (2003) to obtain expected approximate line strengths. Although the line strengths are specifically for fluorescence by Lyα, this influences mainly the lines in the NIR, and their calculation should give an idea of the transitions that are most important. The expected Fe II line strengths are plotted with red lines in Fig. 8.

Although we do not unambiguously detect strong and resolved Fe II lines, the Fe II $\lambda\lambda$ 4924, 5018 lines could be contributing to the He I $\lambda\lambda$ 4922, 5016, 5048 lines (the latter two are blended). As shown in Table C.2, the FWHM velocities of these specific He I lines show a large increase between +14 and +52 d not seen in other He I lines.

At +14 d, two broad features are visible at wavelengths consistent with [Ca II] $\lambda\lambda$ 7292, 7324 (blended with He I λ 7281) as well as with Mg II $\lambda\lambda$ 7877, 7896, although here we cannot rule out contamination from O I λ 7774 to the observed feature. From +20 d we also identify the Ca II H and K lines and the Ca II NIR triplet in emission. The spectrum at +52 d shows significant changes in the line shapes. The Mg II $\lambda\lambda$ 7877, 7896 disappears into the noise, while the Ca II NIR triplet and the blend of [Ca II] $\lambda\lambda$ 7292, 7324 and He I λ 7281 become stronger. The evolution of Ca II and Mg II lines are shown in Fig. B.1 of the Appendix.

In the final spectrum at +52 d, resolved Hα is clearly seen that is significantly narrower (and weaker) than the He I features. The FWHM is $\lesssim$ 1000 km s^{-1} and the centroid is bluehifted by 300 km s^{-1}. The evolution of the region around Hα is also plotted in Fig. B.1. The +52 d Hα line is clearly resolved as it contains 3 − 4 resolution elements. It was also closely inspected in the 2D Keck spectrum and is clearly separated from both a nearby HII region and the galaxy center, which were lying along the slit. However, because of the low number of resolution elements, it is difficult to delineate the continuum from the line exactly and hence to measure the FWHM velocity accurately. We estimate a FWHM velocity of ∼8–900 km s^{-1}.

The non-helium lines are especially interesting as indicators of advanced nucleosynthesis. The most interesting diagnostic lines in this respect are the [O I] $\lambda\lambda$ 6300, 6364 and Mg I] λ 4571. However, even at day +52 when such indicators should become stronger, Mg I] is weak and [O I] is below the noise, if at all present (Fig. 8).

4.3. Host environment properties

One intriguing aspect of SN 2018bcc is the position within the host galaxy, since the supernova is situated relatively far from the center. The host of SN 2018bcc is SDSS J161422.13+355501.3 and does not have a known redshift. Therefore, we use the redshift measured from the SN spectrum (Sect. 4). This galaxy has the following measured SDSS magnitudes: $u = 19.70 \pm 0.07$, $g = 18.66 \pm 0.01$, $r = 18.32 \pm 0.01$, $i = 18.07 \pm 0.01$, $z = 17.94 \pm 0.04$.

Based on the magnitudes of the host galaxy of SN 2018bcc and the position of this SN with respect to the nucleus, it is possible to estimate the metallicity at the SN position. After correcting for extinction and distance modulus, we use the relation provided by Sanders et al. (2013a) that connects the absolute g-band magnitude and the $g - r$ color of the galaxy to its central O3N2 oxygen abundance. We obtained log(O/H)+12=8.39 dex. However, the SN is located in the outskirts of the host, at a projected distance of 7″ along the major axis, which corresponds to 1.04 times the radius of the galaxy, R[10]. Assuming a negative metallicity gradient in the galaxy of −0.47 dex R^{-1} as in Taddia et al. (2015), we derive a metallicity [log(O/H)+12] at the position of the SN of ∼7.9 dex, which is significantly sub-solar (Z = 0.16 Z$_\odot$). This estimate would be even lower if there were projection effects.

SDSS J161422.13+355501.3 is also a source in GALEX General Release 6 (Bianchi et al. 2014), with UV fluxes in the far- and near-UV bands (FUV and NUV, respectively). We obtained the fluxes in a 7.″5 aperture using NED[11] and corrected them for interstellar dust extinction following Salim et al. (2007) for the FUV band. We used the extinction corrected FUV band flux to estimate the star formation rate using the calibration from Salim et al. (2007), and obtain SFR∼ 0.2 M$_\odot$ yr^{-1} (for a Salpeter IMF).

5. Modeling

5.1. Bolometric lightcurve

In order to model the possible powering mechanism of SN 2018bcc with semi-analytical lightcurve models, we construct a bolometric lightcurve from our observations. Due to the fact that we lack multi-band coverage across the EM-spectrum (especially in the UV and NIR), we employ a hybrid approach to construct the bolometric lightcurve.

First we use our spectra to create a quasi-bolometric lightcurve via direct integration of the common integration region from 4000 Å to 8500 Å (excluding the LT spectrum at +3 d that does not cover this region). We then extend this region to the UV and NIR by using our BB fits, going to the left edge of the U-band in the UV at 3300 Å. Following Lyman et al. (2014) we cut off the SED for wavelengths shorter than 2000 Å, since there should be strong line blanketing there. We linearly interpolate from zero flux at 2000 Å to the value of our BB fit at 3300 Å (i.e., the left edge of the typical U-band). We convert the integrated flux from this exercise into bolometric magnitudes and calculate a bolometric correction to the r-band absolute magnitude lightcurve at the epochs of the spectra using the interpolated r-band lightcurve model from Sect. 3.2. The bolometric lightcurve was then created from these bolometric corrections. Details of our methods are explained in Appendix A.

The derived bolometric correction is good enough for our purposes; we want to use this bolometric lightcurve mainly to assess the underlying powering mechanisms. The pseudo-bolometric lightcurve we obtain by applying our derived bolometric correction to the r-band lightcurve is plotted in Fig. A.1. Except for the systematic uncertainties on the distance and MW extinction, all other sources of error are propagated for this figure, with the uncertainty from absolute flux-calibration being dominant. In the proceeding analysis, we add the uncertainty from distance (a large systematic error due to cosmology). We also add the scatter in *all* possible bolometric corrections obtained via varying our assumptions (see Appendix A). Thus, the resulting uncertainty is very conservative. While neither error dominates, the scatter in the bolometric correction is a larger source of error. With these additions, the bolometric luminosity at peak (L_p) is $2.0 \pm 0.8(0.1) \times 10^{43}$ erg s^{-1} and the total radiated

[10] Which was obtained from the SDSS.

[11] The NASA/IPAC Extragalactic Database (NED) is operated by the Jet Propulsion Laboratory, California Institute of Technology, under contract with the National Aeronautics and Space Administration.

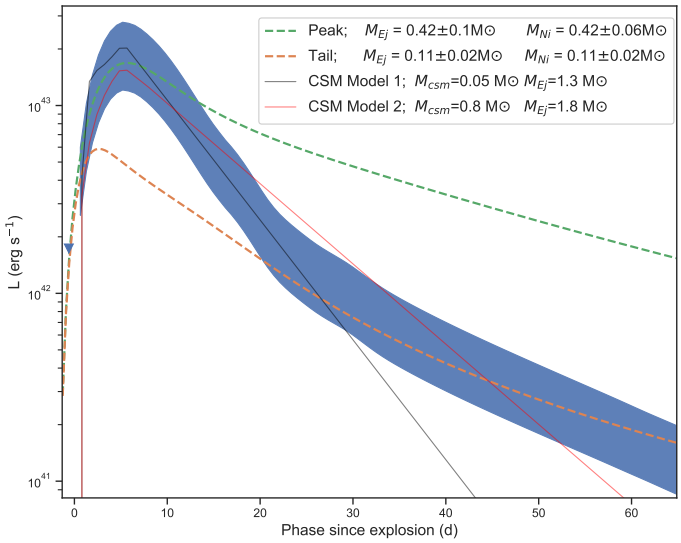

Fig. 10 Arnett (dashed-lines) and CSM model (straight lines) fits to the bolometric lightcurve of SN 2018bcc (blue). For the Arnett models, the bright peak of SN 2018bcc requires a larger mass of ^{56}Ni than the total ejecta mass allowed by the rapidly evolving lightcurve, which is unphysical. Therefore, Arnett models cannot fit both the bright peak and the rapidly declining tail simultaneously, even when accounting for gamma-ray leakage. Instead, we show two examples of CSM interaction powered model fits that can reproduce the bright and rapidly evolving peak of SN 2018bcc, using different parameters describing the CSM. Due to the caveats of these models (see text), we only use them to illustrate that bright and rapidly evolving lightcurves, such as that of SN 2018bcc, can be naturally produced by CSM interaction. The r-band upper limit has been included using the same bolometric correction as in Sect. 5.1.

energy is $2.1 \pm 0.8(0.1) \times 10^{49}$ erg. The error bars in the parenthesis are from the single method described above (and plotted in Fig. A.1), without the larger error from distance and the scatter in all possible values of the bolometric corrections.

5.2. The powering mechanism of SN 2018bcc

While the luminosity of ordinary SE SNe are thought to be powered by the radioactive decay of ^{56}Ni, strongly CSM interacting SNe could be dominated by the luminosity input from shocks created by the collisions between the ejecta and the nearby dense CSM. Certainly for Type Ibn SNe, it is possible that CSM interaction dominates the luminosity input, since we see evidence for CSM interaction in the spectra. In this section we model the bolometric lightcurve of SN 2018bcc using two semi-analytical lightcurve models.

In the first, sometimes referred to as a "simple" Arnett (1982) model, we assume the SN is powered by only the radioactive decay of ^{56}Ni. A working algorithm for this model was presented by Cano (2013). We follow the assumptions of Karamehmetoglu et al. (2017) and use an ejecta expansion velocity of V= 7000 km s^{-1}, a constant effective opacity of $\kappa = 0.07$ cm^2 g^{-1}, and an $E/M_{ej} = (3/10)V^2$ where E is the kinetic energy and M_{ej} is the ejecta mass. In the standard Arnett model, the energy produced by radioactive decay is primarily radiated in the form of gamma-rays that are fully trapped by the ejecta. However, as the opacity drops with expansion, some gamma-rays should escape without thermalizing, thus lowering the observed luminosity. In our modeling, we also take into account the luminosity decrease due to this gamma-ray leakage following the scaling relations of Clocchiatti & Wheeler (1997) and additionally apply the modification for energy loss via positrons (Sollerman et al. 1998), using the same implementation as in Karamehmetoglu et al. (2017).

The result of our fitting is plotted with dashed lines in Fig. 10. Using these assumptions, it is not possible to explain the rapidly evolving lightcurve of SN 2018bcc using radioactive powering alone. Since there cannot be more nickel than the total ejecta mass, attempting to fit the peak requires a high mass of ^{56}Ni and hence too high of an ejecta mass to fit the lightcurve tail. Conversely, lowering the ejecta mass to fit the tail means that even if all of the ejecta were made of ^{56}Ni, there is not enough to power the peak of the lightcurve. (A more realistic ratio of ^{56}Ni to ejecta mass would allow $\sim$2 $M_\odot$ of ejecta that can still fit the tail for the same ^{56}Ni mass.) Thus, it is not possible to get a good fit to the lightcurve of SN 2018bcc with radioactive decay alone.

In order to unconstrain the ejecta mass as much as possible, we allowed the explosion epoch for the Arnett fits in Fig. 10 to vary as long as they were below the pre-explosion limit from the r band, since uncertainty in the explosion epoch is the strongest source of error for ejecta mass. The assumed characteristic ejecta velocity of V= 7000 km s^{-1}, which was obtained for the transitional Type Ibn SN 2010al by Pastorello et al. (2015a), is another source of uncertainty. Higher velocities would lead to higher ejecta masses. However, higher velocities also lead to greatly increased gamma-ray leakage (e.g., Sollerman et al. 1998; Karamehmetoglu et al. 2017). These two effects can combine to produce a reasonable fit to SN 2018bcc with $M_{ej} \gtrsim 2\times$ ^{56}Ni mass, but such a model requires ejecta velocities in excess of 0.1c. Since we lack any evidence to support such high-energy ejecta with relativistic velocities, this scenario seems unlikely.

Since it is not possible to fit the lightcurve with a purely radioactive decay powering scenario using observationally-based reasonable parameters, we turn to CSM interaction as an additional powering scenario that might be able to explain the bright but rapidly evolving lightcurve. In this exercise, we adopt the models of Chatzopoulos et al. (2012) to construct a toy model of CSM interaction to test whether CSM interaction can indeed power the bright and rapidly evolving lightcurve of SN 2018bcc. In this simplified model the luminosity from a forward and reverse shock due to ejecta-CSM interaction is assumed to come from a steady photosphere at some suitable distance. We use the same physically-based assumptions as in Karamehmetoglu et al. (2017) to construct a CSM interaction model to fit Type Ibn SNe.

The complicated nature of CSM interaction means that either changing the parameters in the same model, or modifying the model to take more parameters into account, are possible ways to achieve a model fit. To illustrate this fact we plot two example CSM model fits using different parameter values in Fig. 10 that both produce a bright and rapidly evolving peak. By showing two different example fits, we highlight that the parameters used are not unique.

The CSM models 1 and 2 have reasonable ejecta and CSM masses of 1.3 and 0.05 $M_\odot$ and 1.8 and 0.8 $M_\odot$, respectively, with additional differences in parameters controlling the CSM properties (their details can be found in the Appendix). We emphasize that modifying the parameters that control the nature of CSM interaction could extend the model to also fit the tail. In this exercise we simply wanted to show that, unlike in the radioactive decay powered scenario, a bright and rapidly evolving peak can be powered by CSM interaction using reasonable values.

Presumably, if CSM interaction powers the main peak of the lightcurve, an ordinary SE SN lightcurve with a low ^{56}Ni mass could be hidden underneath. Subtracting the CSM powered lightcurve can then provide an estimate of the ^{56}Ni mass of the underlying "hidden" lightcurve. However, since our spectra show continued evidence of CSM interaction, and no evidence of SN ejecta in the form of broad SN lines or a nebular spectrum with enhanced abundances, we caution that any such combined model would have to predict continued CSM interaction and lack spectral features of ejecta from a SN explosion. Nevertheless, using our CSM models from Fig. 10, we estimate that ~0.03 $M_\odot$ of ^{56}Ni could be powering a possible "hidden" SE-SN lightcurve. A higher ^{56}Ni mass is possible based on the Arnett model fit to the tail, if the CSM interaction is less luminous than our models.

The shock-interaction models of Chatzopoulos et al. (2012) were developed for studying SLSNe with potentially high-mass and extended CSM. The assumptions of their simplified models may not be particularly appropriate for rapidly evolving lower-mass objects, such as Type Ibn SNe. Therefore, in order to move beyond our simple modeling, we make use of our spectra to model the properties of the CSM around SN 2018bcc in the next sections.

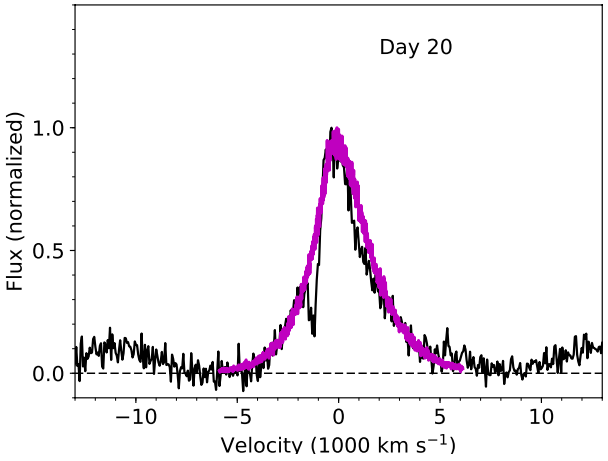

Fig. 11 Comparison of the observed continuum subtracted He I λ 5876 line at day 20 (black) and the calculated line profile due to electron scattering (magenta).

5.3. Modeling the He I line profiles

The spectra of SN 2018bcc also offer insights into the nature of the CSM interaction. An important indicator of strong CSM interaction is the presence of a broad electron scattering wing in the emission lines. As can be seen in Fig. 9, these scattering wings are clearly detected in the strong He I λ 5876 and λ 7065 emission lines up to day 20, where the wings extend to $\sim$ 5000 km s^{-1}. Overall the lines are symmetric; a characteristic of electron scattering. As a result, the maximum extension of the lines are likely coming from electron scattering instead of representing the expansion velocity of the emitting region. However, the slightly bluehifted peaks also seen in Fig. 8 indicate that, in addition to electron scattering, there is macroscopic bulk motion of the emitting region. Although, redshift uncertainty can possibly account for some of the observed blueshift (~300 km s^{-1}; Sect. 2.3), which we consider in the following investigation.

To illustrate this more quantitatively we have modeled the line profile of the day +20 He I λ 5876 line, using an extended version of the Monte Carlo code in Fransson et al. (2014). The result of our modeling is shown in Fig. 11, where we have overplotted our model on top of the continuum subtracted He I λ 5876 line. We obtain an expansion speed of the emitting region of 600 $\pm$ 300 km s^{-1} and an electron scattering optical depth of $\tau_e = 7$ for an assumed electron temperature of $T_e = 15,000$ K. Depending on the assumed temperature, the optical depth scales as $\tau_e \propto T_e^{-1/2}$. A temperature of 7000 K would therefore correspond to $\tau_e \approx 10$.

Given the small number of parameters in the model, the fit is very good. Both the overall shape of the line wings and the bluehift of the peak are well-reproduced. The main discrepancy is the P-Cygni absorption between ~800–1800 km s^{-1}.

The fact that the electron scattering optical depth is large means that any absorption component will be filled in by the scattering as long as the optical depth is $\tau_e \gtrsim 1$. The P-Cygni lines we observe must therefore form at lower τ_e, i.e., in the outer part of the shell, while most of the emission, seen in the $\lambda\lambda$ 5876, 6678, 7065, 7291 lines, should originate at larger τ_e.

The best estimate of the expansion velocity of the line forming region comes from the blue edge of the P-Cygni lines, in particular the lines with a weak emission component, like the He I λ 3889 and λ 4471 lines. On the day 20 spectrum, these lines extend to 1900 $\pm$ 400 km s^{-1}, which we take as the expansion velocity of the CSM. The error is derived by adding in quad the measurement uncertainty with the systematic uncertainty from redshift.

The fact that the velocity from the P-Cygni absorption (1900 $\pm$ 400 km s^{-1}) is larger than that inferred from the line shift of the electron scattering, $\sim$ 600$\pm$300 km s^{-1} means that the emitting region of the photons has a lower velocity than where the P-Cygni absorption arises. Such a case is seen in Eta Carinae, where several velocity components from different parts of the ejecta are present. While most of the ejected material has a velocity of $\sim$ 650 km s^{-1}, a small fraction has velocities up to 3500 – 6000 km s^{-1} (Smith 2008). These can be the result of several separate eruptions with different velocities, as observed e.g., for the pulsational pair instability models in Woosley (2017). However, a range of velocities can also be a result of a single ejection, where a nearly homologous velocity field is achieved after one or two expansion timescales. This type of velocity field is again observed for the ejecta in Eta Carinae (Smith 2006).

Moreover, multi-component velocity fields have been previously observed in Type Ibn SNe and were discussed by Pastorello et al. (2016). As they note, the velocity of the emitting material might not represent the velocity of the deepest ejecta layer. Instead, it could also be coming from the interface between the forward and reverse shocks, effectively hiding the ejecta velocity.

5.4. CSM optical depth and density from He I emissivity

The relative fluxes of the He I lines are of interest for understanding the physical conditions in the CSM. The strongest lines in the optical region are the λ 5876 and λ 7065 lines. Under normal ISM conditions the He I $\lambda\lambda$ 7065/5876 ratio is $\sim$ 0.18 (e.g., Benjamin et al. 1999). However, in SN 2018bcc this ratio is $\sim$ 0.60 at +20 days and $\sim$ 1.01 at +52 days. The He I line ratios depend on density, temperature, and optical depth. In particular, a high optical depth of the λ 3889 line will increase the λ 7065 line relative

Line	Flux ratio relative to the λ 5876 line	
Å	Day +20	Day +52
3889	0.082	0.014
4471	0.056	0.068
4922	0.15	0.34
5018	0.21	0.22
5876	1.0	1.0
6678	0.28	0.26
7065	0.84	1.19
7291	0.21	0.21

Table 2 Line flux ratios measured from the spectra used in Sect. 5.4.

to the λ 5876 line (e.g., Osterbrock & Ferland 2006). Although, other lines are also sensitive to optical depth effects.

To study these effects we have calculated line strengths for different optical depths, electron densities, and temperatures, using atomic data from Benjamin et al. (1999). The temperature and electron densities are assumed to be constant in the emitting region and are mainly important for the role of collisional excitation and de-excitation. As is common, we have used the optical depth of the λ 3889 as a parameter. The model assumes a Sobolev escape probability with homologous expansion velocity. As was discussed in last section, this is a natural choice if the CSM is a result of discrete eruptions. However, as long as the lines are optically thick, which is the case considered here, the escape probability is only weakly sensitive to the velocity field. E.g. if we consider a constant velocity, rather than a homologous expansion, the escape probability is $\beta = 2/(3\tau)$ compared to $\beta = 1/\tau$ in the optically thick limit. The factor $2/3$ comes from the angle averaging.

Table 2 gives the observed line fluxes of the most important lines relative to the λ 5876 line at +20 and +52 days. Our main constraints are the $\lambda\lambda$ 7065/5876, $\lambda\lambda$ 6678/5876 and $\lambda\lambda$ 7291/5876 ratios. These are all well determined to $\lesssim 20\%$. There are also uncertain (but still very useful) estimates from the λ 3889 and λ 4471 lines. Although both lines have strong P-Cygni absorption, their total net emission still provides important constraints in conjunction with the other ratios. When calculating χ^2 in Figs. 12 and 13, He I $\lambda\lambda$ 6678, 7065, 7291 line ratios provided the main constraints while He I $\lambda\lambda$ 3889, 4471 line ratios were used as lower limits since the latter lines are strong in absorption but weak in emission.

Our results are presented in Fig. 12. In the upper panels of Fig. 12, the line ratios relative to the λ 5876 line as function of optical depth, $\tau(3889)$, are shown for two electron densities, $n_e = 10^6 \mathrm{cm}^{-3}$ and $n_e = 10^7 \mathrm{cm}^{-3}$, respectively. In the lower two panels, the line ratios are instead shown as a function of electron density for two different optical depths, $\tau(3889) = 3.1 \times 10^3$ and $\tau(3889) = 3.1 \times 10^4$, and a temperature of $T_e = 7 \times 10^3$. The modeled line ratios (colored lines) are compared to the observed ratios at +20 and +52 days, which are shown as horizontal dashed and dotted lines, respectively, with each color corresponding to a specific line ratio. In the rest of the paper, the line ratios will omit the denominator (λ 5876) for conciseness, i.e., λ 7065/5076 ratio will be λ 7065 ratio.

As we see in the upper panels, the emissivity of the λ 7065 ratio increases from a low value at small optical depths to a value close to one for $\tau(3889) \gtrsim 10^3$, where it reaches a maximum, before decreasing again. The λ 3889 and λ 4471 line ratios become strongly quenched as $\tau(3889)$ increases before subsequently becoming large again as the line ratios approach local thermodynamical equilibrium (LTE) at very high $\tau(3889)$. The same qualitative behavior occurs as function of the electron density as shown in the lower panels. The line ratios are therefore useful as a diagnostic of these parameters.

The black vertical lines in this figure show the best fit values of $\tau(3889)$ or n_e to the observations at +20 days (dashed lines) and +52 days (dotted lines). However, the best fit values of $\tau(3889)$ and n_e depend both on each other and on the electron temperature. In Fig. 13 we show the χ^2 value of the best fit as function of these parameters at +20 and +52 days for $T_e = 7 \times 10^3$ K. There is obviously a strong correlation between the best fit values of $\tau(3889)$ and n_e. Nevertheless, these figures show that the observations strongly indicate high optical depths for the He I λ 3889 line, $\tau(3889) \gtrsim 10^3$, as well as a moderately high electron density, $10^5 \lesssim n_e \lesssim 10^8 \mathrm{cm}^{-3}$. While we found that the observed lines ratios could be fit in a range of T_e between $0.5\text{–}15 \times 10^4$ K, the acceptable range of density and optical depth is not strongly affected by T_e in this range: the best fit CSM parameters are always at high density and optical depth. In addition, $T_e \approx 7 \times 10^3$ K produces the lowest χ^2 values and is roughly in agreement with the estimated BB temperatures at these epochs.

Although we have focused on the optical depth of the λ 3889 line, optical depths of other lines are also larger than one in the region of the $\tau(3889)$–n_e plane favoured by the line ratios. The optical depths vary depending on the level the absorption takes place (e.g., the λ 4471 line originates from the $2\,^3P$ level). For instance, the λ 6678 line, coming from the singlet level $2\,^1P$, is the line which becomes optically thick last of the lines considered, but is still marginally optically thick for the best fit parameters.

Fig. 12 shows us why some He I lines display P-Cygni absorptions while others are dominated by emission. At the high optical depths and densities indicated by our analysis, lines from the lower levels are the ones with the strongest emission. This is a well known result of the branching of emission from higher levels at high optical depth (e.g., Osterbrock & Ferland 2006). E.g., the λ 3889 line into the λ 7065 plus 4.3μm and λ 10830, while the λ 4471 line splits into 1.7μm plus 4.3μm and λ 7065. Therefore, The fact that 'red' lines are the ones showing strong emission is therefore simply explained by the fact that they cannot branch into other lines. Meanwhile, the 'blue' lines are the ones that trap the photons, which then branch into longer wavelengths. Photons scattered by these therefore emerge at longer wavelengths, resulting in P-Cygni absorptions without the strong emission seen in the redder lines.

6. Relation to other Type Ibn SNe

Owing to the increased discovery rate from optical surveys, two comprehensive reviews of Type Ibn SNe have recently been published, P16 and H17, which include 16 and 22 objects respectively, with some overlap. In this section, we compare the results of our analysis to these literature samples of Type Ibn SNe.

Photometrically SN 2018bcc is a typical fast-evolving example of the Type Ibn class. We show this in Fig. 14, which is an augmentation of a figure from H17 (their figure 12), with the risetime, decline slope, and peak magnitude in r band of SN 2018bcc indicated by a blue star. The photometric properties of SN 2018bcc fits within the rest of the sample closer to the faster evolving part of the distribution. Paralleling SN 2010al, the Type Ibn SNe with the best early color information (Pastorello et al. 2015a), SN 2018bcc is blue in color at first, becomes redder, before evolving back to the blue again. A comparable color evolution was also seen for SN 2015U (Shivvers et al.

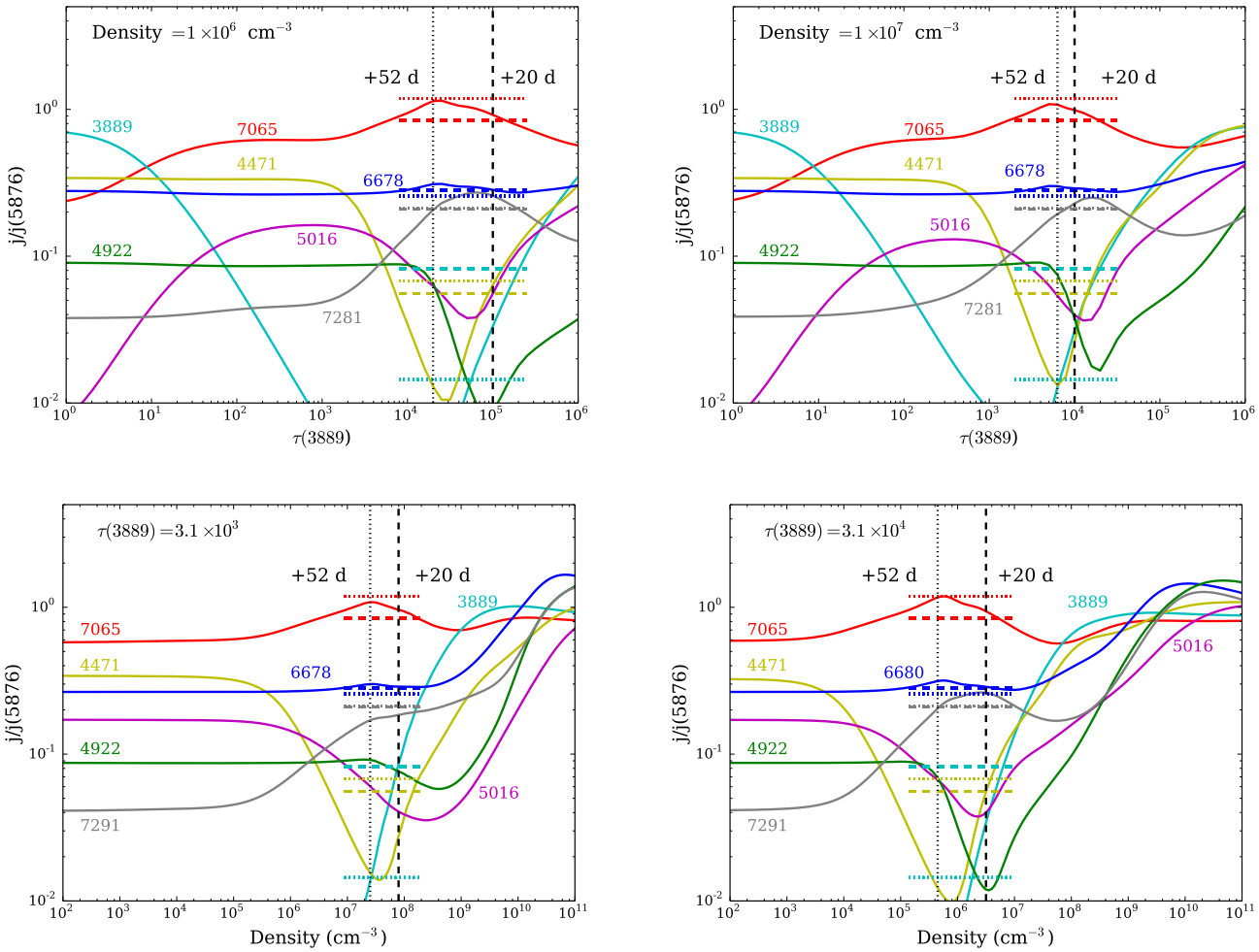

Fig. 12 Emissivities (j) of the most important He I lines relative to the λ 5876 line. The upper panels show this as function of the optical depth in the λ 3889 line for two electron densities, $n_e = 10^6 cm^{-3}$ and $n_e = 10^7 cm^{-3}$, while the bottom panels shows the same as function of the electron density for an optical depth in the He I λ 3889 line, $\tau(3889) = 3.1 \times 10^3$ (bottom left) and $\tau(3889) = 3.1 \times 10^4$ (bottom right). The dashed colored lines give the corresponding observed line ratios for +20 days (dashed lines) and for +52 days (dotted), while the dashed vertical lines show the density and optical depth with the minimum chi square for these values of parameters. In all cases $T_e = 7 \times 10^3$ K.

2016; H17). Similar to the findings in P16, and as also discussed in several papers on other individual Type Ibn SNe, we find that the radioactive decay of ^{56}Ni alone cannot explain the bolometric properties of SN 2018bcc and that an additional luminosity input, such as from CSM interaction, is needed.

It is important to note that the correlations seen in Fig. 14 do not include upper limits, which make the correlations with rise-time unreliable. Luckily, the correlation between decline slope and peak magnitude is not affected by this source of error. From it, we see that brighter Type Ibn SNe tend to decline slightly faster on average, although there is significant scatter that is further impacted by the uncertain contribution of host extinction.

Spectroscopically, the photospheric velocities of the He I lines, as measured from the minimum of the P-Cygni profile, are similar to those of other Type Ibn SNe discussed by P16, with values around $\sim$ 1000 km s^{-1} at 20 to 60 days past peak. Additionally, we also see evidence of a bump blue-ward of ~5500 Å that is likely from a forest of Fe II lines. We also see emission lines from Ca II and Mg II. A relatively strong Mg II emission feature is often detected in Type Ibn SNe (P16), with varying degrees of relative strength of the Mg II lines and potentially the nearby O I line (Fig. 8). Our deep late-time spectra suggest an evolution in the Ca II and Mg II features, with the former becoming much stronger and the latter almost disappearing[12]. This could indicate that the mixed Mg II and O I feature quickly wanes after peak for fast-evolving Type Ibn SNe. Interestingly, LSQ12btw and LSQ13ccw, both very rapidly-evolving Type Ibn SNe, showed a relatively weak mixed feature of Mg and O located around $\sim$ 7700 Å.

We do not see a transformation of the relatively narrow He I emission lines into broader lines ($V \gtrsim 4000$ km s^{-1}) with strong P-Cygni, as was seen in a few Type Ibn SNe (SN 2010al, ASASSN-15ed, SN 2005la, and SN 2015G). These have sometimes been referred to as transitional Type Ib/Ibn SNe, since their spectra evolve to become more similar to ordinary Type Ib SNe in some cases. Instead, we see the lines profiles of the emission

[12] While this evolution was not reported in the samples of P16 and H17, the reason could be the paucity of their late-time spectra.

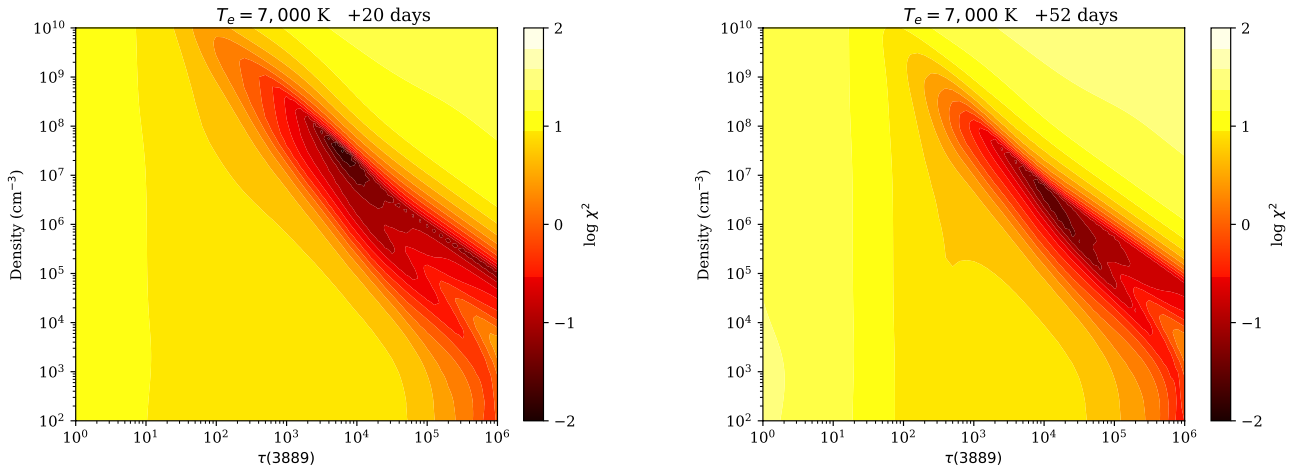

Fig. 13 Contour plots of the χ^2 of the fits at +20 and +52 days as function of the electron density and optical depth in the He I λ 3889 line, τ(3889). The electron temperature was assumed to be $T_e = 7 \times 10^3$ K. When calculating χ^2, the He I λ 7065, λ 6678 and λ 7291 line ratios provide the main constraints, while the λ 3889 and λ 4471 lines ratios are used as lower limits since they have strong P-Cygni absorption and weak net emission.

dominated He I lines become more boxy by day 52, without an obvious strong P-Cygni absorption.

A slight declining trend in the FWHM of the He I lines was observed for SNe 2006jc, 2014av, and 2002ao, which we do not unambiguously detect in SN 2018bcc. This was interpreted by P16 as a decline in the velocity of the shocked gas regions, perhaps resulting from a steeper density profile of the CSM. We note that, alternatively, a declining FWHM could simply mean that the electron scattering depth decreases and therefore the lines become narrower.

We do not detect strong hydrogen features in our spectra before +52 d, though resolved Hα *is* detected in the final spectrum with a line profile that is narrower than the He I lines. Hα and other hydrogen features are sometimes seen in Type Ibn SNe and can be similar in strength to the He I lines.

A relatively strong Mg II emission feature is often detected in Type Ibn SNe (P16), with varying degrees of relative strength of the Mg II lines and potentially the nearby O I line (Fig. 8). Interestingly, the fast-evolving Type Ibn SNe LSQ13ccw and LSQ12btw showed relatively weak Mg II and O I. The mixed feature of Mg and O located around $\sim$ 7700 Å evolves in our spectra and becomes weaker at late times, which could indicate that this feature generally wanes quickly past peak for fast-evolving Type Ibn SNe. Finally, we also detect the Ca II NIR triplet which has been seen for most Type Ibn SNe that have spectral covering at these wavelengths a few weeks after explosion.

7. Discussion

7.1. Two types of Type Ibn SNe?

As discussed in the introduction, H17 pointed to the possible existence of two observational sub-types based on the early He I line profiles. One class shows narrow P-Cygni profiles while the other has He-lines purely in emission[13]. In SN 2018bcc, all He I features show narrow P-Cygni with velocity minima around $\sim$ 1000 km s^{-1} at least up to +14 days. However, in the later spectra, the blue He I features ($<$ 5000 Å) keep their narrow P-Cygni profiles while the redder features such as He I $\lambda\lambda$ 6678, 7065 lose their P-Cygni profiles, which were initially weaker to begin with. Thus, SN 2018bcc cannot cleanly fit into the simple division proposed by H17 based on the presence or lack of the narrow P-Cygni line profiles. This suggests that with higher SNR spectra (especially bluewards of $<$ 5000 Å) the picture might be more complicated. The same spectrum can both show and not show P-Cygni profiles, which has also been noted in H line profiles of Type IIn SNe (e.g., Taddia et al. 2013). Similar to SN 2018bcc, the spectra of the nearby Type Ibn SN 2015G were also found to not fit this simple division (Shivvers et al. 2017).

H17 suggest that the difference between these two observational classes of Type Ibn SNe can be explained by a difference in optical depth; the ones dominated by emission should be optically thin while the ones showing P-Cygni profiles should be optically thick. The mix of scattering dominated P-Cygni lines and emission dominated lines in the spectra of SN 2018bcc shows that this picture is too simplified. As our modeling in Sect. 5.3 shows, the mix of P-Cygni and emission-dominated He I lines in SN 2018bcc are result of the high optical depths and densities in the CSM. In particular, the lines dominated by emission (and lacking a clear P-Cygni at late times), such as the $\lambda\lambda$ 5876, 6678, 7065 lines, are all still optically thick. They are emission dominated because they lack other lines to branch into and not due to being optically thin.

So, how are the P-Cygni lines formed? In SN 2018bcc, the line producing region responsible for the P-Cygni profiles is likely to be in the regions of the CSM where $\tau_e < 1$ (Sect. 5.4). The ionization of He is expected to be caused by UV and X-rays produced at the shock deep in the interaction region. However, the ionized region responsible for the electron scattering, as well as the He ionization and recombination, is likely to have a moderate τ_e. This is the case for a radiative shock where the optical depth of this region is regulated by a balance between the ionizing flux from the shock and the total recombination rate. As discussed in Fransson et al. (2014), $\tau_e \propto V_{shock}^3$, but independent

[13] H17 note that this division may also represent a continuum of Type Ibn SNe with short and long-lived P-Cygni lines.

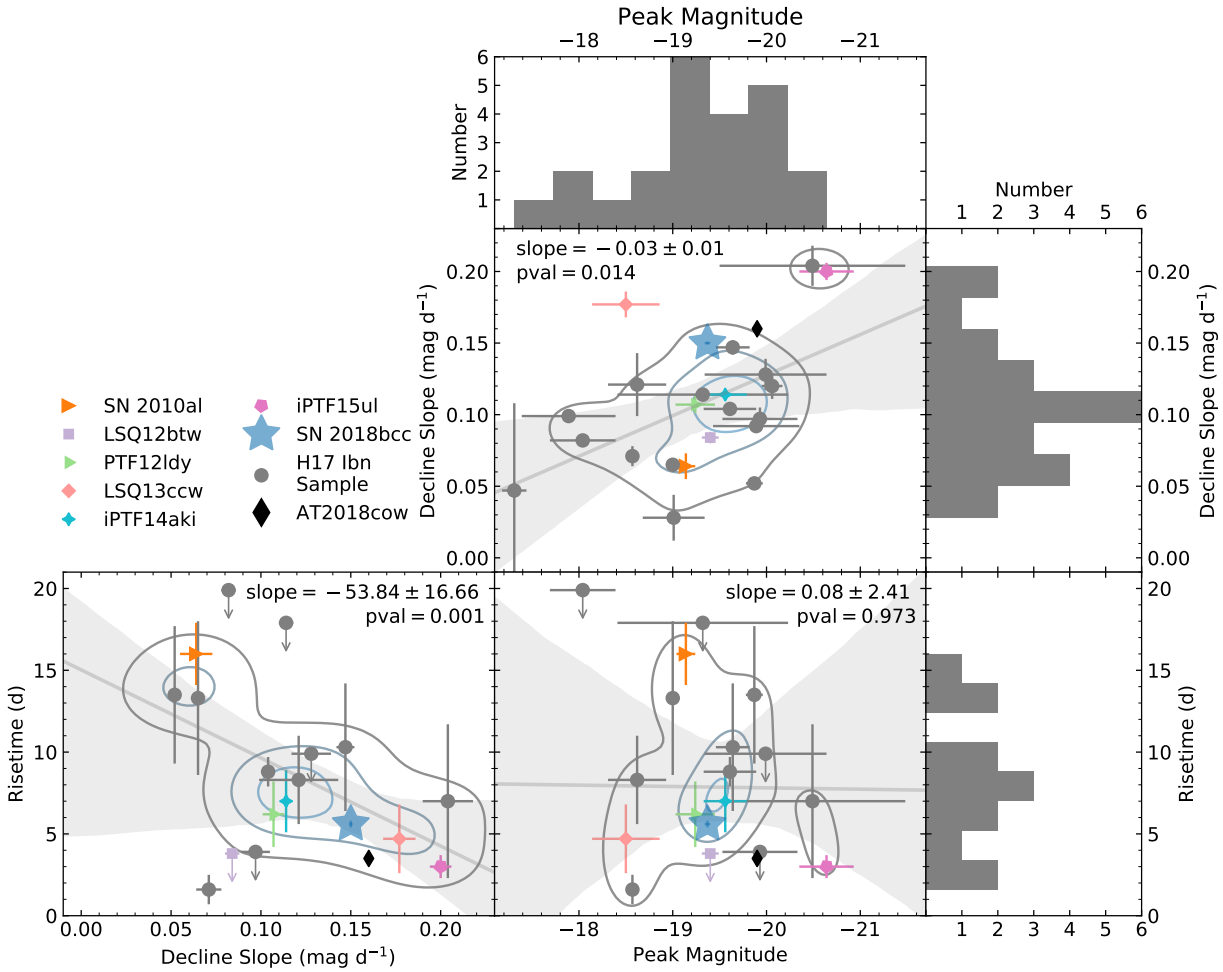

Fig. 14 Comparison of observational properties of SN 2018bcc with the literature sample of Type Ibn SNe from H17, adapted from their figure 12. SN 2018bcc (blue star) and the comparison sample used in this paper are indicated against the rest (gray circles). The results of an unweighted linear regression are shown in gray lines with the given slope and p-value, with the 90% confidence intervals indicated by the shaded regions. A density estimate has been overplotted for each scatter plot using contours. Based on these results, SN 2018bcc seems to be a typical member of the fast-evolving sub-type. The linear regression uncertainties are calculated from the scatter in the data, ignoring the individual errors. The risetime upper limits are not included in the linear regression, density estimates, or the histogram.

of the mass loss rate of the progenitor. A $V_{\rm shock} \lesssim 10^4$ km s^{-1} results in $\tau_{\rm e} \lesssim 10$, which may only correspond to a fraction of the total column density of the CSM. While in this picture most of the emission and electron scattering may be produced by the entire ionized region outside of the shock, the P-Cygni absorption should originate from the outer part of this region where $\tau_{\rm e} < 1$.

X-rays penetrating increasingly further out into the P-Cygni producing region will lead to stronger emission features, which may fill-in the absorption. This can help explain the gradual shift to more emission dominated line profiles we see in the spectral sequence of SN 2018bcc and of Type Ibn SNe in general.

There is some observational evidence for the existence of X-rays from deep in the interaction region in Type Ibn SNe: both SN 2006jc and SN 2010al had X-ray detections. The X-ray lightcurve of SN 2006jc was seen to peak ~100d after the optical (Immler et al. 2008). SN 2010al had only a marginally significant X-ray detection with Swift/XRT (Ofek et al. 2013), but there were indications that the peak occurred well after maximum optical light in this case also.

A late X-ray peak is also expected on theoretical grounds. Assuming that He is singly ionized and a solar abundance of metals by mass (which dominate the X-ray absorption), the ratio of photoelectric absorption at 1 keV to electron scattering is $\sim 10^3$, decreasing approximately as E^{-3}. Then, the fact that $\tau_{\rm e} \approx 5 - 10$ means that the X-ray optical depth can be vary large below 10 keV. This estimate only includes the radial optical depth through the ionized region and not the neutral medium outside this zone or scattering within the ionized zone. The actual X-ray absorption may therefore be even larger. As the column density ahead of the shock decreases with time, the optical depth should also decrease and X-rays may leak out, predominantly at high energy. Clumpiness of the medium can speed up this further (by making lower column-density lines of sight possible). Thus, X-rays that are initially trapped would leak out at

later times, leading to an X-ray lightcurve that peaks after the optical, such as the one that was observed for SN 2006jc.

In an alternative scenario, H17 suggest that a viewing angle effect in non-spherically symmetric CSM, such as a torus, can be responsible for the two spectral classes. In this case, edge-on and face-on views respectively show or hide the P-Cygni profile. Although we propose a different explanation based on theoretical and observational grounds, viewing angle effects in asymmetric CSM could still play a role.

7.2. Risetime and powering mechanism of SN 2018bcc

To date, SN 2018bcc is the best example of a fast Type Ibn SN with a well-sampled early lightcurve. As Table 1 shows, risetimes and the shapes of the rising lightcurves of fast Type Ibn SNe have been uncertain. We find that both the rising lightcurve of the previous best candidate, iPTF15ul, and of SN 2018bcc are compatible with a t^2 powerlaw. A rising powerlaw index of ~2 has been associated with simple expanding fireball models in Type Ia SNe (e.g., Riess et al. 1999). In the simple fireball model, a t^2 powerlaw relationship is expected if the temperature and velocity of the photosphere are nearly constant. The fact that the rise is consistent with the fireball model can offer insights into the CSM environments of Type Ibn SNe and bears further study. In interaction powered SNe with optically thick CSM, the rising lightcurve is likely created by shock breakout occuring inside the CSM (Chevalier & Irwin 2011). The shape of this rise powered by diffusion is then sensitive to the density profile and geometry of the CSM (see e.g., Ofek et al. 2010). Therefore, regularity in the rise of some Type Ibn SNe could be an indication of regularity in these conditions.

Similar to many other Type Ibn SNe, the rapid evolution and brightness of SN 2018bcc cannot be reproduced by a pure ^{56}Ni-powering scenario, without luminosity input from another powering mechanism. In the case of Type Ibn SNe, which are defined by the spectroscopic signs of interaction with a He-rich CSM, a natural explanation for this additional luminosity is CSM interaction. Using a model of shock-interaction powering from Chatzopoulos et al. (2012) we showed that a reasonable mass of dense CSM around the SN could provide the required additional luminosity. We caution that our simplified modeling was performed via visual inspection of the fit for physically plausible values of the model parameters, since we were mainly interested in whether or not CSM interaction could be the potential powering scenario. More sophisticated modeling on the entire Type Ibn SN sample will be required to learn more about the actual values of the model parameters and its limitations.

7.3. CSM interaction properties of SN 2018bcc

In this section, we discuss whether a consistent picture of the CSM around SN 2018bcc has emerged from our study. In Sect. 5.2, we have modeled the CSM properties of SN 2018bcc using both lightcurves and spectra. One way to compare the results from lightcurves and spectra is to estimate the mass-loss rate implied by the analysis or model. However, our lightcurve modeling is based on the work of Chatzopoulos et al. (2012), and was designed for slowly evolving high-mass SNe, such as SLSNe. While the simplifying assumptions in this model may be appropriate for SLSNe, they are less so for rapidly evolving low-mass SNe, such as Type Ibn SNe. One particular issue is that the diffusion time of the model will be overestimated for low-mass SNe, causing the model to prefer fits with artificially lower CSM and ejecta masses (see Clark et al. submitted.). Thus, we only use the model to indicate that CSM interaction is a plausible powering mechanism and not to derive the detailed properties of the CSM. For the latter, we rely on our spectral modeling instead. Nevertheless, we estimate mass-loss rates from lightcurve and spectral based methods to act as a comparison.

Moriya & Maeda (2016) used the peak bolometric luminosities and risetimes of Type Ibn SNe to estimate their explosion properties and CSM densities. For the ejecta density profile assumed in their work, the CSM density parameter D given by their equation 4 requires the observables L_p, peak luminosity, and t_d, the risetime. Using the values from their work and inserting the peak luminosity and risetime of SN 2018bcc, we obtain $D \approx 3.4 \times 10^{15}$ g cm^{-1}, in perfect agreement with the other Type Ibn SNe in their sample. With the wind velocity (v_w), we can also estimate the mass-loss rate of the progenitor as $\dot{M} \approx 4\pi v_w D$, obtaining

$$\dot{M} \approx 0.07 \left(\frac{v_w}{1000 \text{ km s}^{-1}} \right) M_\odot \text{ yr}^{-1} \quad (1)$$

Similarly, our CSM interaction lightcurve models can also be used to estimate the mass-loss rate. Assuming a wind-like CSM, the mass loss rates can be derived using $\dot{M} \approx 4\pi \rho_{csm} R_p^2 v_w$, where R_p is the radius of the constant photosphere assumed in the model and ρ_{csm} is the CSM density in g cm^{-3}. For CSM model 2 from Sect. 5.2 (Fig. 10), we obtain

$$\dot{M} \approx 0.06 \left(\frac{v_w}{1000 \text{ km s}^{-1}} \right) M_\odot \text{ yr}^{-1} \quad (2)$$

Using a typical wind velocity suitable for a WR star ($v_w \sim 1.5 \times 10^3$ km s^{-1}), we obtain ~0.1 $M_\odot$ yr^{-1} for both estimates. Although for the second estimate, the previously noted bias for a lower CSM mass of our model for the case of SN 2018bcc implies that the density, and hence the mass-loss rate, could be higher.

Looking at the spectra, our modeling of the line profile at +52 days in Sect. 5.3 resulted in an optical depth $\tau_e = 8.6(T_e/10^4 \text{ K})$. In principle this provides an estimate of the mass loss rate. Assuming a wind profile for the outflow with velocity V_{exp}

$$\tau_e = \int_{R_{in}}^{R_{out}} \frac{\dot{M}\kappa_e}{4\pi V_{exp} r^2} dr = \frac{\dot{M}\kappa_e}{4\pi V_{exp}} \left(\frac{1}{R_{in}} - \frac{1}{R_{out}} \right) \quad (3)$$

For a gas dominated by singly ionized He $\kappa_e \approx 0.1$. The outflow velocity is uncertain. We therefore scale it to $V_{exp} = 1000$ km s^{-1}, which is in the observed range 600 – 2000 km s^{-1} for the Hα blue shift and the terminal velocity of the P-Cygni profile (Sect. 5.3). We have only weak constraints on the inner and outer radii of the ionized region, R_{in} and R_{out}. If we assume that $R_{in} \ll R_{out}$ only R_{in} is important. As a rough estimate we assume that $R_{in} \approx V_{exp} t \approx 10^3$ km s^{-1} × 46 days $\approx 4.0 \times 10^{14}$ cm. Putting all this together we arrive at

$$\dot{M} \approx 0.68 \left(\frac{V_{exp}}{1000 \text{ km s}^{-1}} \right)^2 \left(\frac{T_e}{10^4 \text{ K}} \right)^{-1/2} \left(1 - \frac{R_{in}}{R_{out}} \right)^{-1} M_\odot \text{ yr}^{-1} \quad (4)$$

When considering this estimate, we note that there are large uncertainties in several of the parameters. While the opacity and outflow speed are probably within a factor two, especially the

inner radius and thickness of the region are highly uncertain. On the one hand, a thinner shell would increase the mass loss rate, while a lower expansion velocity would lower the mass loss considerably. Therefore, Eq. 4 should mainly be considered as an order of magnitude estimate.

The He I optical depths and densities inferred from our modeling in Sect. 5.3 can also provide an estimate of the mass-loss rate. However, because the observed He I lines all come from highly excited levels, estimates of the optical depth require estimates of the fractional populations of these levels. These in turn require detailed modeling of the He I spectrum, including photoionization, recombination, and collisional processes, i.e. a complete modeling of the SN spectrum, which is out of the scope of this paper. Even without this, we find that both spectra and lightcurve based estimates of the mass-loss rate are very high, in the region associated with eruptive mass-loss in massive stars (Smith 2014).

Our spectral modeling offers further insight into the properties of the CSM. Modeling of the He I lines in SN 2018bcc has shown that optical depth and electron density are degenerate and the best fits to the observed line fluxes are all located in a region of high density and optical depth (Sect. 5.4). A high optical depth is also supported by our modeling in Sect. 5.3. As we described in Sect. 7.1, optically thick CSM can help explain the evolution of P-Cygni lines in SN 2018bcc, and probably in Type Ibn SNe.

Based on these results, we conclude that SN 2018bcc has a dense and optically thick CSM environment, with a progenitor that experienced a very high mass-loss rate. Such a high mass-loss rate, combined with the suggestion that the CSM around Type Ibn SNe is in a spatially confined shell (Moriya & Maeda 2016; Hosseinzadeh et al. 2017), suggests a different mechanism than ordinary steady-state line-driven winds as the likely creator of the CSM around Type Ibn SNe. A potential candidate is eruptive mass-loss via some mechanism such as wave-driven super-Eddington winds (Quataert et al. 2016) or the Pulsational Pair Instability (PPI; Woosley et al. 2007; Woosley 2017), which are both expected to lead to the formation of CSM shells. While there are few observational predictions from the acoustic mechanism, Fuller & Ro (2018) predict a mass-loss rate $\sim$0.1 $M_\odot$ yr^{-1}, in line with our estimates for SN 2018bcc. We discuss the PPI in detail in Sect. 7.4.

Narrow ($\lesssim$ 1000 km s^{-1}) but clearly resolved Hα is seen in the final spectrum of SN 2018bcc, though it is blueshifted by 300 km s^{-1} (Appendix, Fig. B.1), representing the systematic redshift uncertainty of SN 2018bcc. It does not show a boxy profile unlike the He I lines in this spectrum. In order to explain the appearance of Hα we consider two cases. In the first case, the ejecta or CSM are catching up with slower and more H-rich material ejected previously. However, in this case one would expect similar widths for the H and He lines, contrary to the observations. Alternatively, this H-rich material may be located much further out, and is instead being photo-ionized by X-rays produced in the interaction region. This would explain the lower velocity of the H-rich material. We discuss this possibility further in the next section. We note that a successful model of CSM interaction in SN 2018bcc would need to both explain the peculiarities of the He I lines profiles, as well as the late-time rise of narrower Hα.

7.4. Comparison with pulsational pair-instability supernova models

Woosley (2017, hereafter W17) discussed the possibility that Type Ibn SNe may be the result of pulsational pair instability (PPI) SNe. These have an origin in high-mass stars with He-core masses between 30–64 $M_\odot$, corresponding to ZAMS masses of 70–140 $M_\odot$ (with a large uncertainty due to unknown mass-loss rates). As such massive stars approach the pair instability region, they undergo violent nuclear flashes that send strong enough pulses to eject any H-envelope, as well as parts of the He-core. The number of pulses and the duration between each pulse varies strongly with the He-core mass. The durations range from hours to a few thousand years, with more energetic pulses leading to a larger interval (W17). Interaction between shells ejected in these pulses, or if energetic enough an ejection in itself, can create SN-like transients referred to as PPI SNe.

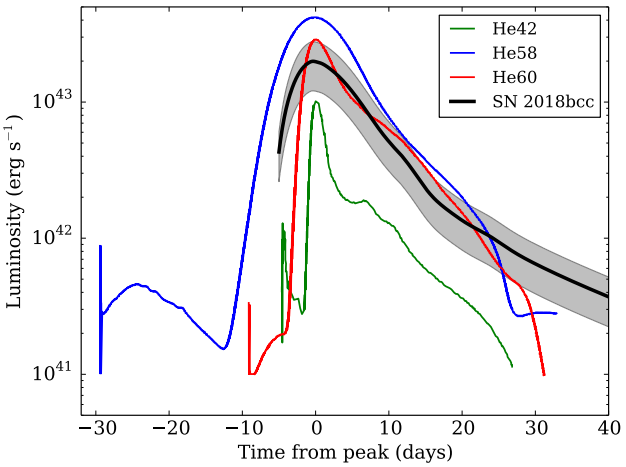

Fig. 15 Comparison of the bolometric lightcurve of SN 2018bcc, including errors (grey, shaded region), with the bolometric lightcurves of the He42 (green), He58 (blue) and He60 (red) models from W17.

Both the luminosities and the shape of the lightcurves of the resulting SNe vary strongly with the He-core mass. In particular, the peak luminosity and the rising part of the lightcurve vary strongly between different models, which is a result of both the energy in the pulses and the time interval between pulses. Unlike pair instability SNe, PPISNe leave behind a massive (> 30 $M_\odot$) remnant that (eventually) undergoes CC, either directly forming a black hole or possibly exploding as a SN. Due to the altered composition of the remnant, a neutrino driven explosion is thought to be unlikely (W17). Hence, the possible contribution of a final CC SN is ignored in the proceeding discussion.

Although suggested before, there have been few direct comparisons of model PPISN lightcurves with Type Ibn observations. We have therefore used our bolometric lightcurve for a comparison with the W17 models of He stars. The models are named such that the He-core mass of a model is indicated by the number; e.g., He50 is a 50 $M_\odot$ He-core mass model. In Fig. 15 we compare our bolometric lightcurve with the lightcurves of the He42, He58, and He60 models from W17 (his fig. 6). It is important to stress again that the lightcurves of the models vary significantly with He-core mass in a non-linear way. In fact, the lightcurves of the high-mass models (He58 and He60) are formed in a different way than the lightcurve of the low-mass model (He42).

The He42 model is included as an example at the lower mass-range for a PPISN and was among the models discussed by W17 as a possible candidate for a Type Ibn SN. The duration of pul-

sations in the lower mass-range models is only a few days and hence the energetics are lower. In total, He42 ejects 2.65 $M_\odot$ of material in several pulses that power the lightcurve seen in Fig. 15. The luminosity of the He42 model is a factor of $\sim$ 5 lower than that of SN 2018bcc. The total radiated energy is similarly lower; $\sim 3.9 \times 10^{48}$ ergs for the He42 model while it is $\sim 2.1 \times 10^{49}$ ergs for SN 2018bcc. The effective temperature at the peak was 23×10^4 K in the model compared to the observed $\sim 15 \times 10^4$ K. These differences with SN 2018bcc also apply to the He40 and He44 models.

For intermediate-mass models He48–He54, the lightcurves all have multiple peaks as a result of colliding shells emitted within months to a few years before collapse. Hence, despite the fact that the peak luminosities of these models are in the range of that of SN 2018bcc, the overall widths of these lightcurves are far too broad. Therefore, these models are excluded for SN 2018bcc.

Higher-mass models, such as He58 and He60, have fewer but more energetic pulses and a much longer duration between the first and second pulse, on the order of thousands of years. However, similar to the lower-mass models, the later pulses occur on a time scale of days and the ejected shells merge on a short time scale resulting in a smooth lightcurve. Therefore, as can be seen in Fig. 15, the lightcurves of the He58 and He60 models are in better agreement with the observed bolometric luminosity of SN 2018bcc and are consistent with it given the limitations of the models. These lightcurves do not show the first pulse which occurred thousands of years prior that is predicted to be optically faint.

The He58 and He60 models have total radiated energies of $\sim 4.4 \times 10^{49}$ ergs and $\sim 1.9 \times 10^{49}$ ergs, respectively. This is more similar to the total radiated energy for SN 2018bcc, $\sim 2.1 \times 10^{49}$ ergs, than the lower mass He42 model. In the latter pulses, they expel 4.8 $M_\odot$ and 2.0 $M_\odot$ of material for the He58 and He60 models, respectively[14]. They also have effective temperatures in the range of 8,000–12,000 K, which is consistent with the observed temperatures for SN 2018bcc (Fig. 7).

The ejecta velocity is another important diagnostic. For the low-mass models, the photospheric velocities are expected to be in the range of 2000–4000 km s^{-1}. Meanwhile for He58 and He60, the resulting velocity only varies between 2500 – 3000 km s^{-1}. The He lines in SN 2018bcc have FWHM velocities in the range of the PPISN models (Sections 4.1 and 5.3). Although, the observed bulk velocity can be lower due to CSM interaction (Sect. 5.3).

While this comparison is very interesting, there are a number of caveats when comparing observations to the models. The largest uncertainty in the observed lightcurves comes from the bolometric correction estimate, due to the lack of UV and NIR data. We have tried to correct for this when calculating the bolometric correction, but there are likely to be considerable uncertainties, as shown by the shaded area in Fig. 15. Nevertheless, the observational uncertainties are relatively minor compared to those of the models.

Comparing different model calculations (e.g., W17; Yoshida et al. 2016; Marchant et al. 2018; Leung et al. 2019), there is broad agreement in terms of energies, number of pulses, and ejected masses. However, there are considerable quantitative differences between models in the literature for the same helium core mass. Furthermore, small differences in He core mass can cause large difference in the lightcurves for the same model calculations, since lightcurve behavior is very sensitive to the He core mass. These one-dimensional models cannot account for instabilities caused by shell interactions, which are likely to be important and to modify the hydrodynamic structure. When comparing with observations, additional uncertainty comes from the fact that the lightcurves of the W17 models are only bolometric, with no color information, and the only opacity source included when calculating the lightcurves is electron scattering and line absorption is neglected. Since all of these factors are important, differences by a factor of two or more are not unexpected.

Nevertheless, there are many agreements between the observational properties of SN 2018bcc and theoretical predictions for PPISNe. In addition to what has been mentioned previously, the appearance of the narrow Hα line at late times can be readily accounted for; it may originate from a more distant shell produced by an earlier ejection, possibly the first pulsation, which ejected most of the hydrogen envelope. We infer a relatively low metallicity for the host galaxy of SN 2018bcc, in agreement with observations by Hosseinzadeh et al. (2019) for several other Type Ibn SNe. Line-driven stellar winds are less efficient at low metallicity, and hence massive stars can more easily survive past the Main-Sequence with larger envelope masses, which are necessary for PPISNe. The late decline of SN 2018bcc and several other fast Type Ibn SNe which seem to lack a radioactive decay tail is also readily explained in the PPISN scenario[15]. Finally, the most important test for the PPISN scenario is that the ejected material should not show enhanced abundances from elements resulting from advanced nucleosynthesis. Despite the fact that a few Type Ibn SNe evolve to show more ejecta-like spectra, we do not detect evidence of SN ejecta or enhanced abundances of elements from advanced nucleosynthesis in the spectra of SN 2018bcc, matching previous observations of a few other fast Type Ibn SNe (see e.g., Pastorello et al. 2015b). Thus, some luminous and fast Type Ibn SNe with these characteristics are attractive candidates to be PPISN explosions, even if other Type Ibn SNe may not be. Additionally, the eventual CC of the remnant, which we did not consider in this discussion due to the large unknowns, may be able to produce ejecta-like spectra seen in some Type Ibn SNe.

One of the predictions of PPI is the depletion of oxygen. Thus, a lack of strong oxygen in late-time spectra (like what we see in SN 2018bcc), can also be a litmus test for PPI in Type Ibn SNe. Interestingly, the late-time spectra of SN 2006jc also lack oxygen, similar to most other Type Ibn SNe. Even in SN 2015G, which is one of the few Type Ibn SNe with more ejecta-like late time spectra, the oxygen line flux was much lower compared to ordinary SE SNe (Shivvers et al. 2017).

Observations that can further test the PPISN scenario for Type Ibn SNe include a study of early and late-time brightening in Type Ibn SNe, as either pulsations or shell-interaction can lead to pre and post SN brightening. However, since the time between pulsations and the duration of pulsations varies widely between hours and days to thousands of years, a statistical study is necessary. On the modeling front, lightcurves from two-dimensional models with realistic stellar envelopes and evolution are needed for a fruitful comparison to observations.

7.5. Progenitor of SN 2018bcc

Type Ibn SNe have been suggested to be the CC of massive Wolf-Rayet (WR) stars exploding into dense and He-rich CSM. Like

[14] The first pulse expels $\sim$10 $M_\odot$, which should now be located at several hundred to a few thousand AU.

[15] Although, the ultimate fate of the remnant in producing a CC SN is unknown.

for other Type Ibn SNe in literature, the CSM around the progenitor of SN 2018bcc would have to have been ejected via a mechanism with a very high mass-loss rate. The SN also seems to be powered by CSM interaction, with little ^{56}Ni. In this progenitor scenario, a normal CC SN explosion could be hidden beneath the CSM interaction powered lightcurve. Even if it came out that there is less ^{56}Ni than expected, one possible way to explain a low ^{56}Ni mass while still having a CC SN could be via fall-back onto the central compact object. However, looking at the available observational evidence, we cannot conclude that this progenitor scenario is the only possibility.

SN 2018bcc is located in a low metallicity environment. It seems to be powered by CSM interaction, with little or no ^{56}Ni, and is a rapidly evolving and fading SN with a relatively low total radiated energy of $\approx 2.1 \times 10^{49}$ erg (low for an interaction powered SN). The spectra neither show direct evidence of nucleosynthesis nor fast, SN-like, ejecta (velocities $\sim$10,000 km s^{-1}). Therefore, it is also worth exploring the possibility that SN 2018bcc, and perhaps other fast Type Ibn SNe, are not terminal CC SNe. As discussed in Sect. 7.4, if the progenitor of SN 2018bcc was a massive star in a low-metallicity environment, the lightcurve and interaction properties (from the spectra) could be the result of the collision of CSM shells ejected via *some* mechanism, such as the PPI. In this alternative scenario, the progenitor of SN 2018bcc is a very massive star whose remnant may even collapse to form a blackhole, either directly or as a failed SN (e.g., Gerke et al. 2015).

In the case of PS1-12sk, the only Type Ibn SN to have exploded outside of an elliptical galaxy with deep limits on the star formation rate, Sanders et al. (2013b) and Hosseinzadeh et al. (2019) evoked the possibility that the progenitor was a white-dwarf system. For SN 2018bcc, the rapidly declining lightcurve and lack of ^{56}Ni also makes thermonuclear explosions an unlikely progenitor scenario. As noted in the study of Type Ibn SN host environments by Hosseinzadeh et al. (2019), all Type Ibn SNe may not even share a common progenitor. Various progenitor systems can create interaction powered SNe with strong He emission lines. It seems that in the case of SN 2018bcc, either the CC of a WR star or non-terminal ejection into a dense, He-rich CSM, are possible progenitor scenarios. PPI is one plausible mechanism that can give rise to either. Ultimately, the nature of the progenitors of fast Type Ibn SNe remains unknown.

7.6. AT2018cow

As seen in Fig. 14, SN 2018bcc is a fast Type-Ibn SN that is otherwise ordinary. Remarkably, the photometric properties of the enigmatic transient AT2018cow are not that different from SN 2018bcc or other fast Type Ibn SNe. Furthermore, AT2018cow developed post-peak He I emission features that look similar to many other Type Ibn SNe (Perley et al. 2019), along with several other spectral similarities. These similarities were highlighted in a recent paper by Fox & Smith (2019), who discussed the CSM interaction scenario for AT2018cow in detail (however see Wang & Li 2019). We note that in our basic modeling, SN 2018bcc could be mostly ^{56}Ni powered for characteristic ejecta velocities $\gtrsim 0.1c$. Although we lack any evidence for such relativistic ejecta in SN 2018bcc, and thus discount this possibility, AT2018cow had an early broad feature with just such a high velocity (Perley et al. 2019). If CSM interaction can explain the observables of AT2018cow, then, just like other Type Ibn SNe, it might be a viable PPISN candidate. In this scenario, very high velocity ejecta seen at early times could be coming from the CC of the remnant shortly after the cessation of pulsations, while the CSM interaction in the ejected shells can explain other observables. If AT2018cow is indeed similar to fast Type Ibn SNe, further study of this nearby enigmatic object might also illumine the mystery surrounding Type Ibn SNe, or vice versa.

8. Conclusion

We have studied the rapidly evolving Type Ibn SN 2018bcc and have obtained the best constraints on the combined risetime and shape of the rising lightcurve for this type of fast Type Ibn SN. It has a risetime of $5.6^{+0.2}_{-0.1}$ days in the restframe with a rising powerlaw index close to two. Photometrically and spectroscopically, SN 2018bcc seems to be a typical but fast-evolving member of the Type Ibn SN class.

Modeling of the bolometric lightcurve suggests that ^{56}Ni cannot be the sole powering-mechanism for this SN, even when accounting for gamma-ray leakage. An additional luminosity input is needed, which we show with our simple modeling can readily be provided by CSM interaction. Our spectral modeling suggests that the He I line profiles have strong electron scattering wings and thus are likely not representing the expansion velocity. Furthermore, the observed He I line flux ratios suggest optically thick CSM and a high electron density, $10^5 \lesssim n_e \lesssim 10^8$cm^{-3}. In addition, the He I lines are all optically thick even at +52 days.

The CSM around SN2018bcc is likely produced by a high mass-loss rate of $\sim$0.1 $M_\odot$ yr^{-1}, which suggests an alternative formation mechanism, such as eruptive mass-loss. We also do not find strong evidence of CC SN signatures. As a result, SN 2018bcc could be the result of a CC SN interacting with a He-rich CSM ejected in an eruptive episode, or possibly the interaction of CSM shells ejected via an eruptive mechanism, such as the PPI mechanism. We showed that given all of the available evidence, SN 2018bcc (and by extension other fast Type Ibn SNe), are viable PPISN candidates.

We found that the simple spectral classification scheme proposed by H17, based on the evolution of the narrow P-Cygni profiles of He I, does not neatly fit SN 2018bcc. We see He I features both with and without narrow P-Cygni profiles in the same spectra, with P-Cygni profiles present in the blue part and emission dominated features in the red part of the spectrum. Furthermore, their explanation that optical depth effects can explain the discrepancy is found to be too simplified, since all lines are still optically thick. Instead, the branching of emission from higher levels in a He atom at high optical depths is likely responsible for the creation of P-Cygni profiles. Lines that lack branching possibilities become emission dominated, e.g., redder lines like λ 7065.

The nature of Type Ibn SNe remains an ongoing mystery. There are even possible associations to extreme events such as AT2018cow, which has been shown to share many observational similarities to the class. We reiterate that more sophisticated modeling on a large sample of Type Ibn SNe is required to answer questions regarding their progenitors, CSM conditions, and powering mechanisms. As of today, observations are lacking to undertake this type of population study for Type Ibn SNe (often done for other SN sub-types). Primarily, there is a lack of early-time photometric observations that can constrain the shape of the rise and peak of these objects, and virtually no color information for the early lightcurves except for a few specific cases (see e.g., Hosseinzadeh et al. 2017). The lack of early time data also makes estimating the explosion epoch difficult, which is a necessary step for lightcurve modeling. Since Type Ibn SN lightcurves decline rapidly, we often also lack nebular spectroscopy which might be able to tell us more about the ejecta and SN properties,

such as expansion velocities. Finally, there have been no systematic exploration of the CSM interaction in Type Ibn SNe in radio and X-rays, as has been deeply studied for Type IIn SNe for instance.

This paper was written with the aim of reporting early results from the ZTF survey with an example of a unique rapidly-evolving SN discovered shortly after the start of the public ZTF survey in March 2018. As the case of SN 2018bcc shows, robotic surveys like the ZTF can be used to discover a sample of well-observed candidates required to undertake a sample study of Type Ibn SNe.

Acknowledgements. We gratefully acknowledge support from the Knut and Alice Wallenberg Foundation and the Swedish Research Council. Based on observations obtained with the Samuel Oschin Telescope 48-inch and the 60-inch Telescope at the Palomar Observatory as part of the Zwicky Transient Facility project. Major funding has been provided by the U.S National Science Foundation under Grant No. AST-1440341 and by the ZTF partner institutions: the California Institute of Technology, the Oskar Klein Centre, the Weizmann Institute of Science, the University of Maryland, the University of Washington, Deutsches Elektronen-Synchrotron, the University of Wisconsin-Milwaukee, and the TANGO Program of the University System of Taiwan. The Oskar Klein Centre is funded by the Swedish Research Council. This research is partially based on observations made with the Nordic Optical Telescope, operated by NOTSA at IAC using ALFOSC, which is provided by the IAA. Some of the data presented herein were obtained at the W.M. Keck Observatory, which is operated as a scientific partnership among the California Institute of Technology, the University of California, and NASA; the observatory was made possible by the generous financial support of the W.M. Keck Foundation. Some of the data presented herein were obtained with the Liverpool Telescope operated on the island of La Palma by Liverpool John Moores University in the Spanish Observatorio del Roque de los Muchachos of the Instituto de Astrofisica de Canarias with financial support from the UK Science and Technology Facilities Council. This work is partly based on observations made with DOLoRes@TNG. This research made use of Astropy, a community-developed core Python package for Astronomy (Astropy Collaboration, 2018) IRAF, is distributed by the National Optical Astronomy Observatories, which are operated by the Association of Universities for Research in Astronomy, Inc., under cooperative agreement with the National Science Foundation. The python version which was used, PyRAF, is a product of the Space Telescope Science Institute, which is operated by AURA for NASA. SED Machine is based upon work supported by the National Science Foundation under Grant No. 1106171. We would like to thank E. Ofek for his comments on the manuscript.

References

Abbott, B. P., Abbott, R., Abbott, T. D., et al. 2017a, ApJ, 848, L13
Abbott, B. P., Abbott, R., Abbott, T. D., et al. 2017b, Phys. Rev. Lett., 119, 161101
Arcavi, I., Hosseinzadeh, G., Howell, D. A., et al. 2017, Nature, 551, 64
Arnett, W. D. 1982, ApJ, 253, 785
Bellm, E. C. 2016, PASP, 128, 084501
Bellm, E. C., Kulkarni, S. R., Barlow, T., et al. 2019a, PASP, 131, 068003
Bellm, E. C., Kulkarni, S. R., Graham, M. J., et al. 2019b, PASP, 131, 018002
Bellm, E. C. & Sesar, B. 2016, pyraf-dbsp: Reduction pipeline for the Palomar Double Beam Spectrograph, Astrophysics Source Code Library
Benjamin, R. A., Skillman, E. D., & Smits, D. P. 1999, ApJ, 514, 307
Bianchi, L., Conti, A., & Shiao, B. 2014, Advances in Space Research, 53, 900
Blagorodnova, N., Neill, J. D., Walters, R., et al. 2018, PASP, 130, 035003
Cano, Z. 2013, MNRAS, 434, 1098
Cenko, S. B., Fox, D. B., Moon, D.-S., et al. 2006, PASP, 118, 1396
Chatzopoulos, E., Wheeler, J. C., & Vinko, J. 2012, ApJ, 746, 121
Chevalier, R. A. & Fransson, C. 2017, Thermal and Non-thermal Emission from Circumstellar Interaction, 875
Chevalier, R. A. & Irwin, C. M. 2011, ApJ, 729, L6
Clocchiatti, A. & Wheeler, J. C. 1997, ApJ, 491, 375
Contardo, G., Leibundgut, B., & Vacca, W. D. 2000, A&A, 359, 876
Coulter, D. A., Foley, R. J., Kilpatrick, C. D., et al. 2017, Science, 358, 1556
Drout, M. R., Chornock, R., Soderberg, A. M., et al. 2014, ApJ, 794, 23
Flewelling, H. A., Magnier, E. A., Chambers, K. C., et al. 2016, arXiv e-prints, arXiv:1612.05243
Foley, R. J., Smith, N., Ganeshalingam, M., et al. 2007, ApJ, 657, L105
Fox, O. D. & Smith, N. 2019, arXiv e-prints, arXiv:1903.01535
Fransson, C., Ergon, M., Challis, P. J., et al. 2014, ApJ, 797, 118
Fremling, C., Sharma, Y., Kulkarni, S. R., et al. 2018, The Astronomer's Telegram, 11688, 1
Fremling, C., Sollerman, J., Taddia, F., et al. 2016, A&A, 593, A68
Fuller, J. & Ro, S. 2018, MNRAS, 476, 1853
Gerke, J. R., Kochanek, C. S., & Stanek, K. Z. 2015, MNRAS, 450, 3289
Graham, M. & Zwicky Transient Facility (ZTF) Project Team. 2018, in American Astronomical Society Meeting Abstracts, Vol. 231, American Astronomical Society Meeting Abstracts #231, 354.16
Hosseinzadeh, G., Arcavi, I., Valenti, S., et al. 2017, ApJ, 836, 158
Hosseinzadeh, G., McCully, C., Zabludoff, A. I., et al. 2019, ApJ, 871, L9
Immler, S., Modjaz, M., Landsman, W., et al. 2008, ApJ, 674, L85
Karamehmetoglu, E., Taddia, F., Sollerman, J., et al. 2017, A&A, 602, A93
Kasliwal, M. M. 2012, PASA, 29, 482
Kasliwal, M. M., Nakar, E., Singer, L. P., et al. 2017, Science, 358, 1559
Leung, S.-C., Nomoto, K., & Blinnikov, S. 2019, arXiv e-prints, arXiv:1901.11136
Lusk, J. A. & Baron, E. 2017, PASP, 129, 044202
Lyman, J. D., Bersier, D., & James, P. A. 2014, MNRAS, 437, 3848
Magnier, E. A., Schlafly, E. F., Finkbeiner, D. P., et al. 2016, arXiv e-prints, arXiv:1612.05242
Marchant, P., Renzo, M., Farmer, R., et al. 2018, arXiv e-prints, arXiv:1810.13412
Masci, F. J., Laher, R. R., Rusholme, B., et al. 2019, PASP, 131, 018003
Moriya, T. J. & Maeda, K. 2016, ApJ, 824, 100
Nicholl, M., Berger, E., Kasen, D., et al. 2017, ApJ, 848, L18
Ofek, E. O., Fox, D., Cenko, S. B., et al. 2013, ApJ, 763, 42
Ofek, E. O., Rabinak, I., Neill, J. D., et al. 2010, ApJ, 724, 1396
Oke, J. B., Cohen, J. G., Carr, M., et al. 1995, PASP, 107, 375
Oke, J. B. & Gunn, J. E. 1982, PASP, 94, 586
Osterbrock, D. E. & Ferland, G. J. 2006, Astrophysics of gaseous nebulae and active galactic nuclei (University Science Books)
Pastorello, A., Benetti, S., Brown, P. J., et al. 2015a, MNRAS, 449, 1921
Pastorello, A., Hadjiyska, E., Rabinowitz, D., et al. 2015b, MNRAS, 449, 1954
Pastorello, A., Mattila, S., Zampieri, L., et al. 2008, MNRAS, 389, 113
Pastorello, A., Smartt, S. J., Mattila, S., et al. 2007, Nature, 447, 829
Pastorello, A., Wang, X. F., Ciabattari, F., et al. 2016, MNRAS, 456, 853
Patterson, M. T., Bellm, E. C., Rusholme, B., et al. 2019, PASP, 131, 018001
Perley, D. A. 2019, PASP, 131, 084503
Perley, D. A., Mazzali, P. A., Yan, L., et al. 2019, MNRAS, 484, 1031
Quataert, E., Fernández, R., Kasen, D., Klion, H., & Paxton, B. 2016, MNRAS, 458, 1214
Riess, A. G., Filippenko, A. V., Li, W., et al. 1999, AJ, 118, 2675
Rigault, M., Neill, J. D., Blagorodnova, N., et al. 2019, arXiv e-prints, arXiv:1902.08526
Salim, S., Rich, R. M., Charlot, S., et al. 2007, ApJS, 173, 267
Sanders, N. E., Levesque, E. M., & Soderberg, A. M. 2013a, ApJ, 775, 125
Sanders, N. E., Soderberg, A. M., Foley, R. J., et al. 2013b, ApJ, 769, 39
Schlafly, E. F. & Finkbeiner, D. P. 2011, ApJ, 737, 103
Shivvers, I., Zheng, W., Van Dyk, S. D., et al. 2017, MNRAS, 471, 4381
Shivvers, I., Zheng, W. K., Mauerhan, J., et al. 2016, MNRAS, 461, 3057
Sigut, T. A. A. & Pradhan, A. K. 2003, ApJS, 145, 15
Smith, N. 2006, ApJ, 644, 1151
Smith, N. 2008, Nature, 455, 201
Smith, N. 2014, ARA&A, 52, 487
Smith, N. 2017, Interacting Supernovae: Types IIn and Ibn, 403
Sollerman, J., Leibundgut, B., & Spyromilio, J. 1998, A&A, 337, 207
Steele, I. A., Smith, R. J., Rees, P. C., et al. 2004, in Society of Photo-Optical Instrumentation Engineers (SPIE) Conference Series, Vol. 5489, Proc. SPIE, ed. J. Oschmann, Jacobus M., 679–692
STScI development Team. 2018, synphot: Synthetic photometry using Astropy, Astrophysics Source Code Library
Taddia, F., Sollerman, J., Fremling, C., et al. 2015, A&A, 580, A131
Taddia, F., Stritzinger, M. D., Sollerman, J., et al. 2013, A&A, 555, A10
Wang, S.-Q. & Li, L. 2019, arXiv e-prints, arXiv:1905.12623
Whitesides, L., Lunnan, R., Kasliwal, M. M., et al. 2017, ApJ, 851, 107
Woosley, S. E. 2017, ApJ, 836, 244
Woosley, S. E., Blinnikov, S., & Heger, A. 2007, Nature, 450, 390
Yaron, O. & Gal-Yam, A. 2012, PASP, 124, 668
Yoshida, T., Umeda, H., Maeda, K., & Ishii, T. 2016, MNRAS, 457, 351
Zackay, B., Ofek, E. O., & Gal-Yam, A. 2016, ApJ, 830, 27

Appendix A: Constructing the bolometric lightcurve

There are three standard methods of constructing a bolometric lightcurve for CC SNe. In the simplest method, the SED is integrated directly (typically using trapezoidal integration), as much as observations permit, and the resulting flux is converted to a quasi-bolometric lightcurve that only accounts for the light in the observed part of the SED. This method is the best when an abundance of observations across the electro-magnetic (EM) spectrum exists for an object.

In the second method, the direct integrated quasi-bolometric lightcurve is extrapolated into the IR and UV by using a combination of fits to the SED (commonly using a blackbody) to estimate parts that are outside of the observed range. Typically a correction is then applied to the blackbody fit to account for heavy line blanketing present in the UV, which is usually not sampled by the observations (Lusk & Baron 2017). This integrated flux can be converted to a bolometric luminosity using the known distance to the SN.

A third method involves calculating a bolometric correction to the observed SED when observations are limited. These corrections are calculated from another property, usually color, and calibrated using well observed (and nearby) SNe so that a simple parametrized relation between color and the bolometric correction is empirically calculated (see e.g., Lyman et al. 2014). However, such a parametrized relation does not yet exist for Type Ibn SNe. As a result, creating a pseudo-bolometric lightcurve for a Type Ibn SN often entails obtaining photometry across the EM spectrum.

Appendix A.1: Steps for SN 2018bcc

In order to create the bolometric lightcurve, we first use our spectra to create a quasi-bolometric lightcurve via direct integration. We use the common range from 4000−8500 Å for direct integration, but we had to remove the LT spectrum as it does not extend beyond 7500 Å. However, since this spectrum is very close in time to the SEDM spectrum (1.5 days in the restframe), we do not lose much information in this way.

We then extend this region to the UV and NIR by using our BB fits. We integrate the BB fits from 3300 − 4000 Å to include the UV up to the left edge of the U-band and from 8500 Å to effectively infinity to include the NIR. Following other authors (e.g., Lyman et al. 2014) we cut off the SED for wavelengths shorter than 2000 Å, since there should be strong line blanketing there. We then interpolate from zero flux at 2000 Å to the value of the BB fit at 3300 Å (the left edge of the typical U-band), as most optical lightcurves of SNe extend to this range, and show it to be well-fit by a blackbody (see e.g., Lyman et al. 2014).

We convert the integrated flux from this exercise into bolometric magnitudes and calculate a bolometric correction to the r-band absolute magnitude lightcurve at the epochs of the spectra. Next, we employ the secondary method and find a simple linear relation between the bolometric corrections we calculated and the $g-r$ color at the same epochs, following the approach of Lyman et al. (2014). The relation between the $g-r$ band and the bolometric correction is plotted in Fig. A.1. We find that a flat (zeroth order) linear fit best describes the relation between the bolometric corrections and the $g-r$ color at the same epochs; a bolometric correction $\approx -0.12 \pm 0.02$ mag. We also tested using first and second degree polynomials to characterize this relation and find that our results do not change.

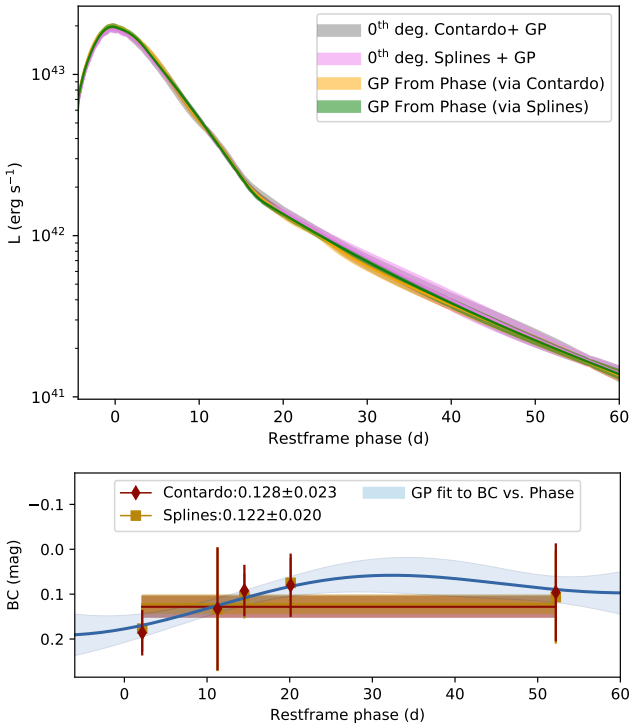

Fig. A.1 **Top:** The bolometric lightcurve of SN 2018bcc. The results from methods discussed in Sect. 5.1 are plotted with different colors and agree within the uncertainties. **Bottom:** Fits to the bolometric correction (BC) as a function of phase, obtained via methods discussed in Sect. 5.1 and Appendix A. The resulting bolometric lightcurve from these methods are plotted in the top panel.

Since a zeroth order correction is preferred using the $g-r$ color, we also look for a relation between phase and bolometric correction using the interpolated $r-$band lightcurve, which yield the same result. Additionally, we use GP regression to learn the relationship between phase and bolometric-correction and calculate a bolometric lightcurve this way. The resulting bolometric lightcurve is very similar to using a zeroth order bolometric correction as a function of color or phase. Thus, we use our simple bolometric correction to calculate the bolometric lightcurve, as illustrated in Fig. A.1.

Finally, we also tested the effects of varying our assumptions when deriving the bolometric correction from the spectra. These tests included using just a simple BB fit, as well as varying the assumptions in the UV, and still found that the resulting bolometric lightcurves were all similar to our desired accuracy.

Appendix B: Figures

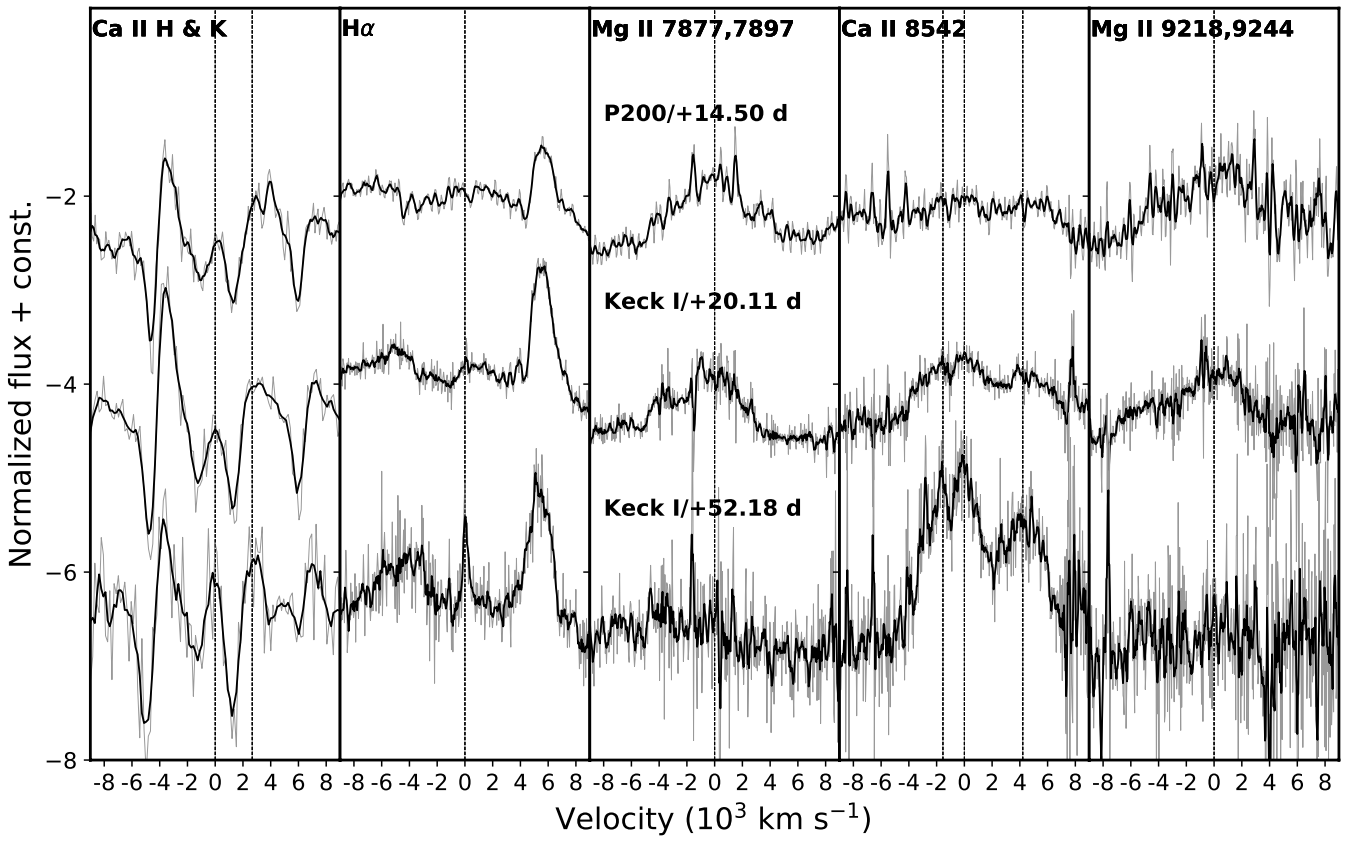

Fig. B.1 Line evolution of prominent Ca II, Mg II lines and Hα. While the Mg II lines fade by +56d, the Ca II features become stronger with time. Hα has been blueshifted by 300 km s^{-1} to match the line centroid.

Appendix C: Tables

Table C.1. Spectral observations

JD-2,458,000 (days)	Phase[a] (days)	Telescope	Instrument	Range (Å)	Resolution[b] (R)
233.83	2.19	P60	SEDM	3575–8629	∼100
235.54	3.80	LT	SPRAT	3782–7521	∼350
243.50	11.28	NOT	ALFOSC	3333–9112	∼360
246.92	14.50	P200	DBSP	3198–9878	∼1423
252.89	20.11	Keck	LRIS	2897–9679	922 ± 34
287.00	52.18	Keck	LRIS	2900–9674	905 ± 26

[a]Restframe days since peak.

[b]Resolving power $R = \lambda/\Delta\lambda$. Values without error bars are the nominal R at the central wavelength for the instrumental set-up used, obtained from the webpage of the respective instrument. The R values with uncertainties are the "seeing-corrected" versions measured from sky spectra at an average effective wavelength of ∼5900 Å.

Table C.2. FWHM and P-Cygni absorption velocities inferred from fitting different lines present at $t > +14$ d. Velocities are spaced with a comma and refer to the fits made on the +14 d, +20 d and +52 d spectrum (P200, first and second Keck spectrum), respectively and refer to the atomic line reported in the first column. Systematic redshift uncertainty of ∼300 km s^{-1} applies while typical measurement uncertainties are ∼200–300 km s^{-1} based on noise.

Line (Å)	P-Cygni maximum absorption (km s^{-1})	Terminal velocity (BVZI) (km s^{-1})	FWHM (km s^{-1})
He I 3889	925, 953, 1350	1914, 1830, 1618	1830, 1860, 1040[a]
He I 4471[b]	800, 845, 1174	1550, 1750, 1850	1020, 1380, 1790[a]
He I 4922[c]	834, 1087, -	1400, 1590, -	1107[a], 704, 2920[a]
He I 5016[d]	1157, 1221, -	1745, 1954, -	755 , 721, 2600[a]
He I 5876	1000, 1020, -	1600, 1356, -	3000, 3020, 3000
He I 6678	990, 1070, -	1470, 1428, -	1950, 2080, 1650
He I 7065	1060, - , -	1645, - , -	2520, 2100, 1871[a]

[a]Uncertain measurements due to the lower SNR of the spectrum at those wavelengths

[b]Possibly contaminated by Mg II λ 4481 line.

[c]Possibly contaminated by Fe II λ 4924 line.

[d]Possibly contaminated by He I λ 5048 and Fe II λ 5018 lines.